DIPLOMARBEIT

Second Harmonic Generation in Mid-Infrared Quantum Cascade Lasers with Surface Gratings

ausgeführt zum Zwecke der Erlangung des akademischen
Grades eines
Diplom-Ingenieurs

unter der Leitung von

a.o. Univ.Prof.Dr. Gottfried Strasser
Institut für Festkörperelektronik

eingereicht an der Technischen Universität Wien
Fakultät für Elektrotechnik und Informationstechnik

von

Hermann Detz

Mat.Nr. 0125152
Trautsohngasse 1
A-2170 Poysdorf

Wien, im September 2007

Betreuer:
Dipl. Ing. Maximilian Austerer
a.o. Univ. Prof. Dr. Gottfried Strasser

Abstract

Since their first demonstration in 1994 quantum cascade lasers (QCLs) [1] represent a permanently growing field of research. Now in 2007 these devices are already available commercially. In contrast to conventional laser diodes QCLs are unipolar devices which rely on light emission caused by intraband transitions of electrons. The subband states and therefore the emission wavelength of the device can be engineered within a wide range by varying the thickness of layers in a semiconductor heterostructure. Fields of application are the generation of light in the mid- and far-infrared domain, the later one also known as the terahertz region (THz). This corresponds to wavelengths of several μm to several 100 μm.

Nonlinear effects, such as second harmonic generation (SHG) allow to access a wider range of wavelengths. These effects are an interesting way to study nonlinear behavior in materials. This work summarizes an approach to improve the efficiency of SHG in gallium-arsenide/aluminium-gallium-arsenide ($GaAs/Al_xGa_{1-x}As$) based QCLs by the use of phase-match gratings, etched in the waveguide. Grating periods from 22 μm to 30 μm were realized and characterized. Although no clear relation between grating period and nonlinear behavior could be found, conversion efficiencies of up to 46.1 $\mu W/W^2$ have been measured.

Zusammenfassung

Seit der ersten Realisierung im Jahre 1994 stellen Quantenkaskaden-Laser (QCLs) [1] ein ständig wachsendes Forschungsgebiet dar. Heute im Jahr 2007 sind sie bereits kommerziell erhältlich. Im Gegensatz zu herkömmlichen Laserdioden handelt es sich um unipolare Bauelemente, welche auf der Lichterzeugung in Folge Intrabandübergängen von Elektronen basieren. Die Subband-Zustände und damit die emittierte Wellenlänge können durch variieren der Schichtdicken in Halbleiterheterostrukturen eingestellt werden. Anwendungsgebiete sind die Lichterzeugung im mittleren und fernen Infrarot, wobei letzterer auch oft als Terahertz Bereich (THz) bezeichnet wird. Das entspricht Wellenlängen im Bereich von einigen μm bis zu einigen 100 μm.

Nichtlineare Effekte, wie die Frequenzverdoppelung (SHG) erlauben das Einstellen der Wellenlänge in einem grösseren Bereich. Des weiteren stellen sie eine Möglichkeit dar, nichtlineares Verhalten von Materie zu untersuchen. Diese Arbeit beschreibt einen Versuch, die Effizienz der Frequenzverdoppelung in Gallium-Arsenid/Aluminium-Gallium-Arsenid ($GaAs/Al_xGa_{1-x}As$) basierten QCLs durch Phasenanpassungsgitter, welche in den Wellenleiter geätzt wurden, zu erhöhen. Es wurden Gitterperioden zwischen 22 μm und 30 μm realisiert und charakterisiert. Obwohl kein eindeutiger Zusammenhang zwischen Gitterperiode und nichtlinearem Verhalten gefunden werden konnte, wurden Konversionseffizienzen von bis zu 46.1 $\mu W/W^2$ gemessen.

Contents

Chapter 1

Introduction

Quantum Cascade Lasers (QCLs) are coherent light sources that cover the mid-infrared and terahertz regions of the electromagnetic spectrum. [1, 2] In contrast to conventional semiconductor lasers the emission wavelength is a design parameter that results from confined states in quantum wells. Furthermore QCLs are unipolar devices. Only electrons are used for light generation. By cascading more active regions it is possible to create more photons per electron.

In 1996, two years after the first demonstration, continuous wave (cw) operation could be achieved.[3] Lasing at room temperature was shown first in the InGaAs/InAlAs material system and later on also for GaAs/$Al_xGa_{1-x}As$ based devices.[4, 5] Also continuous wave operation was presented for these two material systems. [3, 6]

Up to date wavelengths down to $3.05\mu m$ have been demonstrated in the InGaAs/InAlAs/AlAs and in the InAs/AlSb material systems.[7, 8] QCLs based on GaAs/$Al_xGa_{1-x}As$ can be used for mid-infrared and terahertz emission. But due to the lower bandoffset between well and barrier material, wavelengths much shorter than $10\mu m$ cannot be reached from intersubband transitions.[9]

1.1 Motivation for Second Harmonic Generation

Linear processes in QCLs are well understood and various designs both of the active region and the waveguide have already been realized. Obviously the linear theory is sufficient to describe the basic operation. Therefore it might be permitted to ask, why all the efforts are made to study nonlinear effects in such devices.

As the following chapters will show, the $GaAs/Al_xGa_{1-x}As$ material system does not allow fundamental emission based on intersubband transitions much below $10\mu m$. Second and third order effects would provide access to an extended wavelength range, although at much lower efficiencies.

By the use of difference frequency generation it is possible to get emission in the terahertz range from a dual wavelength mid-infrared QCL that shows strong nonlinearities. [10]

Apart from these reasons second harmonics generation is a good approach to investigate nonlinear effects. It can be used in experiments to prove theoretic models and simulations on nonlinear behaviour and to deepen our understanding.

1.2 Outline

The first part of this thesis explains the quantum mechanical effects that lead to coherent emission in cascaded semiconductor heterostructures. Confinement in quantum wells, formation of allowed bands and interaction between electromagnetic waves and matter are discussed to get an idea of the funcional principles.

On this basis the design process of the active region in such a device is treated. Also confinement of the electromagnetic modes in a waveguide structure is covered.

Knowing how a QCL device should look like, the next chapter presents the fabrication process. The growth of the heterostructure and the lithographic

methods to define the waveguide structure are explained.

After that nonlinear processes in QCLs are investigated. The quantum mechanical origin of second harmonic generation (SHG) and additional design issues need to be explained. Furthermore a concept to enhance the efficiency of the SHG process with surface gratings is presented.

Chapter 2

Quantum Mechanics in Semiconductors

The term quantum mechanics suggests that in contrast to classical mechanics the energy scale is not continuous. Amounts of energy may only be multiples of a certain irreducible value.

First of all the band structure of III-V semiconductor compounds is explained. Based on that, methods to solve eigen value problems in the conduction or valence bands are presented. When applied to superlattices, eigenstates that are responsible for charge transport and radiative as well as non-radiative transitions can be identified.

To concentrate on the essential ideas and knowing that the next chapters deal with one dimensional problems, models or calculations in this chapter are shown in one dimension only, wherever it is applicable.

2.1 Bandstructure of $Al_xGa_{1-x}As$

Electrons of lower atomic orbitals are strongly bound to the core and therefore they don't contribute to interatomic bonds or charge transport. In other words electronic properties of matter are determined only by electrons of the outermost orbitals.

In the case of III-V semiconductor compounds such as GaAs the cation

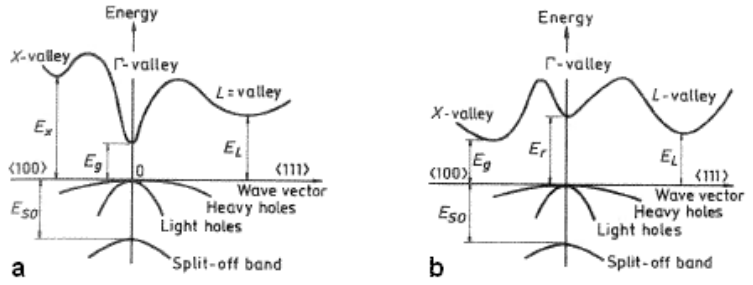

Figure 2.1: Bandstructure of $Al_xGa_{1-x}As$. For Al concentrations below 0.45 the compound is a direct semiconductor, as shown in part a. If the Al content exceeds 0.45, the X-valley lies below the Γ-valley, which makes the compound an indirect semiconductor. [12]

(Ga in this case) adds 3 electrons to the highest orbital, while additional 5 arise from the anion. These 8 electrons form sp^3 hybridized levels which are equivalent to each other and therefore form tetrahedral bonds. [11]

A common property of III-V compounds is the fact, that the top of the valence band is located at the Γ point, which marks the center of the Brillouin zone. Valence bands are mainly defined by the anions, therefore GaAs and AlAs show the same structure of the valence band. [11]

Figure 2.1 shows the bandstructures for two $Al_xGa_{1-x}As$ compounds with different Al content. GaAs as well as $Al_xGa_{1-x}As$ up to 45% of Al are direct semiconductors. That means the lowest point of the conduction band and the topmost point of the valence band, which is the Γ point as mentioned above, are placed at the same value of the momentum (k=0). At 300K there is a bandgap of 1.424eV for GaAs. The direct energy gap of the ternary compound $Al_xGa_{1-x}As$ is roughly linear dependent on the Al content. For an Al content of 45% the bandgap calculates to 1.985eV. Compounds with an Al content of more than 45% usually aren't used in optoelectronic devices because the Γ valley moves up and the material becomes an indirect semidonductor, with the lowest state in the conduction band at the X point. [12]

2.2 Schrödinger's Equation

While in classical mechanics any state of any given system is defined by the solutions of the associated Hamilton Equation, in quantum mechanics some additional considerations need to be included. According to de Broglie, particles can be treated as waves and vice versa. Therefore Hamilton's Equation must be modified to fit for waveform solutions. This leads to Schrödinger's Equation, which cannot be derived from more fundamental laws. It can be obtained by asking for conditions, an equation needs to meet, in order to fit for particle and waveform solutions. [13]

Equation 2.1 shows Schrödinger's Equation for one dimension, with the simplifying assumption of a potential term that is constant in time. It is a linear partial differential equation because Ψ doesn't occur in higher powers. Hence also linear combinations of solutions satisfy the equation. Solving this equation returns a set of eigenvalues and associated eigenfunctions. While the wavefunction resulting from the eigenvalue problem has no physical meaning, the square of it can be interpreted as the probability to find a particle at a certain position. Hence large amplitudes of the wavefunctions correspond to regions where it is likely to find a particle. When talking of solutions to Schrödingers's Equation later on in this thesis, the particles of interest are electrons or holes. [13]

$$\left[-\frac{\hbar^2}{2m}\frac{\partial}{\partial z} + V(z)\right]\Psi(z,t) = \iota\hbar\frac{\partial\Psi(z,t)}{\partial t} \tag{2.1}$$

The most simple solutions satisfying this equation are plane waves. Unfortunately they are not very useful when it comes to real problems because they describe particles that are not localized in space. Reasonable solutions need to meet the condition shown in equation 2.2. [13]

$$\int |\Psi(z,t)|^2 dz = 1 \tag{2.2}$$

Simply said if an eigenvalue problem for a particle is calculated it has to be somewhere. As explained above the term $|\Psi(z,t)|^2$ in equation 2.2 can be identified as propability function and therefore the integral over the whole

simulation space must be equal to 1.

2.3 Operations on Eigenfunctions

As mentioned above eigenfunctions don't have a meaning in real space but the square of them is a measure of likeliness to find particles at a certain position. Operators can be used to connect these probability densities with measured variables. The expressions in angle brackets correspond to the expectation values of the measurands. Equations 2.3 - 2.5 list the most important operators that are used in the following chapters. [13]

$$\langle x \rangle = \int \Psi^* x \Psi dx \qquad = \langle \Psi | x | \Psi \rangle \tag{2.3}$$

$$\langle E \rangle = \int \Psi^* \iota\hbar \frac{\partial \Psi}{\partial t} + V\Psi dx \qquad = \langle \Psi | \iota\hbar \frac{\partial}{\partial t} + V | \Psi \rangle \tag{2.4}$$

$$\langle p \rangle = \int \Psi^* (-\iota\hbar) \frac{\partial \Psi}{\partial x} dx \qquad = \langle \Psi | - \iota\hbar \frac{\partial}{\partial x} | \Psi \rangle \tag{2.5}$$

These expressions can only be evaluated in an analytical way when dealing with simple problems. Most often numeric methods performed by computers are used.

2.4 Semiconductor Heterostructures

The term semiconductor heterostructure stands for a configuration consisting of different materials with different band gaps. Two example materials are shown in figure 2.2a. When put together conduction and valence band align in a way that there is no offset between the fermi energies of the two parts. This situation is sketched in figure 2.2b.

In general two types of semiconductor heterostructures are distinguished. Type-I structures show electron and hole confinement in the same layers, whereas electrons and holes are confined in complimentary layers in type-II heterostructures, due to the alignment of the energy bands. Figure 2.3

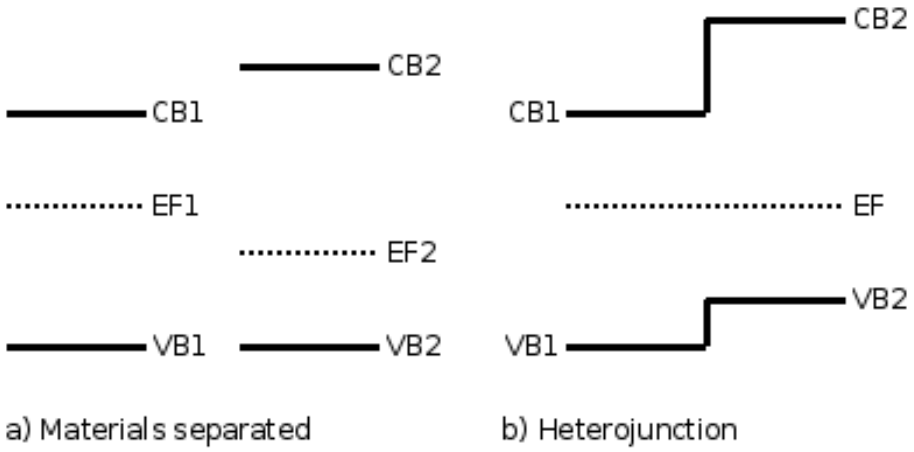

Figure 2.2: Band Alignment in Heterostructures

shows valence and conduction band edges of the two possible well types. [14] Although type-II interband quantum cascade lasers have also been demonstrated, this chapter concentrates on type I because all experiments presented in the following chapters are based on this type. [15]

All the work presented in chapters 3 and 5 is based on n-doped heterostructures, which means that radiative transitions are caused by electrons. As a consequence of the band alignment the well height in the valence band is about half the height in the conduction band. Therefore wells show less bound states in the valence band and carrier transitions are mostly due to phonon emission or absorption. Hence the considerations in the following chapters only include states and transitions in the conduction band.

The basic building blocks for more complex models of intersubband lasers are quantum wells with finite barriers, which are discussed in the next section. Quantum cascade lasers are based on superlattices, which are in fact sequences of barriers and wells. Therefore the basic simulation methods for these structures are shown in section 2.4.2. As the purpose of this section is only to show how eigenstates in semiconductor heterostructures are calculated, time dependent aspects aren't discussed.

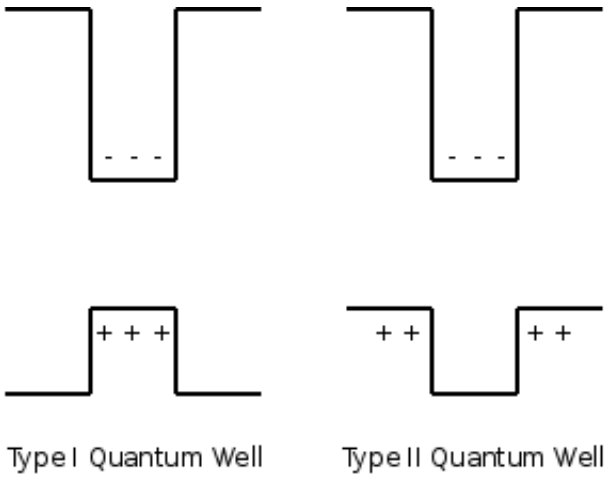

Figure 2.3: Type I and Type II Quantum Well. In type-I wells electrons and holes are are confined in the same well, while in type-II wells they are confined in complimentary layers

2.4.1 Finite Quantum Well

Figure 2.4 sketches the conduction band in a quantum well structure with finite barriers. Schrödinger's Equation must be solved for three different regions, labeled as A, B and C in the figure. From a mathematic point of view infinite barriers outside the regions A and C are necessary. Direct influence of these infinite barriers on the quantum well can be avoided by assigning infinite width to the regions A and C.

Schrödinger's Equation can be written for all three regions (Equations 2.6 - 2.8). Because of the infinite barriers at both sides the wavefunction and it's first derivative must tend to zero at these points, which can be located at $\pm\infty$ as mentioned above. Furthermore both the wavefunction and it's derivative must be continuous at the borders between region A, B and C.

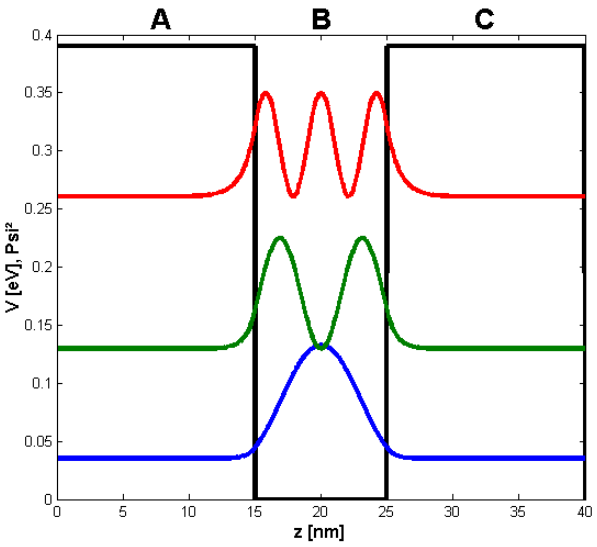

Figure 2.4: GaAs quantum well (10nm) in $Al_{0.45}Ga_{0.55}As$ barriers (15nm). The squared eigenfunctions of the bound states are plotted overlapping with the conduction band edge of the heterostructure.

$$-\frac{\hbar^2}{2m^*}\frac{\partial}{\partial z^2}\Psi(z) + V\Psi(z) = E\Psi(z) \qquad z \leq -\frac{d}{2} \tag{2.6}$$

$$-\frac{\hbar^2}{2m^*}\frac{\partial}{\partial z^2}\Psi(z) = E\Psi(z) \qquad -\frac{d}{2} \leq z \leq \frac{d}{2} \tag{2.7}$$

$$-\frac{\hbar^2}{2m^*}\frac{\partial}{\partial z^2}\Psi(z) + V\Psi(z) = E\Psi(z) \qquad z \geq \frac{d}{2} \tag{2.8}$$

Possible solutions are growing or decaying exponential terms and because of linearity superpositions of these, like sine and cosine terms. Using an exponential function with parameter κ for regions A and C and a cosine function with parameter k for region B as an ansatz, the constants k and κ can be calculated. This universal ansatz is shown in terms 2.9 - 2.11.

$$\Psi(z) = Ae^{\kappa z} \qquad z \leq -\frac{d}{2} \tag{2.9}$$

$$\Psi(z) = B\cos(kz) \qquad -\frac{d}{2} \leq z \leq \frac{d}{2} \tag{2.10}$$

$$\Psi(z) = Ce^{-\kappa z} \qquad z \geq \frac{d}{2} \tag{2.11}$$

Equations 2.12 and 2.13 show possible wavevectors for well and barrier. States with an energy lower than the barrier show a wavevector κ and can be expressed as evanescent waves. Because the wavevector k is proportional to $\sqrt{E}$ thinner wells show eigenvalues with higher energies and vice versa. The probability to find a particle inside the barrier is rather low but anyway important. When the decaying evanescent field reaches another well, quantummechanic tunneling is possible, as the particle is located in both wells at a certain probability. This is the main transport mechanism in superlattice structures described later on.

$$k = \frac{\sqrt{2m_B^* E}}{\hbar} \tag{2.12}$$

$$\kappa = \frac{\sqrt{2m_{A,C}^*(V-E)}}{\hbar} \tag{2.13}$$

Figure 2.4 shows the bound states of a 10nm wide GaAs quantum well with 15nm wide $Al_{0.45}Ga_{0.55}As$ barriers. Even eigenstates can be attributed to symmetric wavefunctions whereas the wavefunctions of odd eigenstates have a root at $z = 0$ and therefore are called antisymmetric.

The relation shown in terms 2.14 and 2.15 is due to the boundary conditions between the regions A, B and C, where the first equation is used for states with even symmetry and the second one for odd states. [16]

$$k \tan\left(\frac{kd}{2}\right) - \kappa = 0 \tag{2.14}$$

$$k \cot\left(\frac{kd}{2}\right) + \kappa = 0 \tag{2.15}$$

2.4.2 Superlattice Structures

Starting from the simple square well problem as explained in the preceding section, the next step would be placing two square wells next to each other in a way that they are separated by a finite barrier. This problem differs from the first by two interfaces which result in four additional equations to be solved. Such a structure shows eigenvalues, that are different from the eigenvalues of the single wells. Also it is noteworthy that the eigenfunctions are spread over both wells with values above zero in the barrier region.

The equations used in section 2.4.1 can also be used to find eigenvalues and eigenfunctions for more complex potentials like superlattices. As for every additional layer two more conditions need to be met, finding solutions requires more calculational effort.

A well known method used to calculate eigenstates of arbitrary superlattice structures is the so called shooting method. By the use of finite differences instead of differentials Schrödinger's Equation can be rewritten as shown in equation 2.16. If the wave function is known at $z - \delta z$ and z, it's value for $z + \delta z$ can be calculated.

$$-\frac{\hbar^2}{2m^*}\left[\frac{\Psi(z+\delta z) - 2\Psi(z) + \Psi(z-\delta z)}{(\delta z)^2}\right] + [V(z) - E]\,\Psi(z) = 0 \tag{2.16}$$

As mentioned above usually infinite barriers are set at both ends of the structure to be calculated, the wave function must be equal to zero at these points. Starting from one of these points a second point can be guessed by the use of symmetry arguments explained in section 2.4.1. Also the number of roots is given by the index of the state. In an iterative process eigenfunctions are calculated point by point and the energy is varied until the eigenfunction

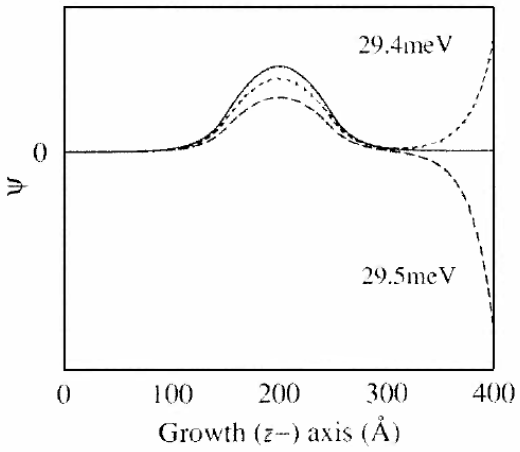

Figure 2.5: Shooting Method, from [16]

converges to a finite value at the last point. In figure 2.5 this iterative process is sketched for the ground state of a quantum well. The dashed lines arise from tries which didn't converge for the right border of the simulation interval. The solid line represents a valid solution for the eigenvalue problem. [16]

To get results that are in good agreement with measurements, additional effects like the non-parabolicity of the bandstructure that is caused by the valence bands must be taken into account. [11]

2.5 Electron - Photon Interaction

When discussing optoelectronic devices it is first necessary to get an idea of how electrons and photons can interact. The purpose of this section is to write about the basic mechanisms, namely absorption, spontaneous emission and stimulated emission. Because the latter one is the basic action in lasers, it's treated in a separate section.

Often a semi classical approach is used, where electromagnetic waves are treated like particles called photons. The relation between the angular frequency of the electromagnetic wave and the energy of the photon is given

by equation 2.17. [17]

$$E = \hbar\omega \tag{2.17}$$

2.5.1 Transition Rates

On one hand Schrödinger's Equation allows to calculate the electron's states while on the other hand electromagnetic waves can be described by the use of Maxwell's Equations. These two systems of equations can be coupled by assuming a harmonic perturbation of Hamilton's Operator which describes an electric dipole formed by the atomic core and the electron. For an electromagnetic wave given by the term 2.18 the perturbation of the potential term is shown in equation 2.19. [17]

$$E(t) = E_0 \cos(\omega t) \tag{2.18}$$

$$H' = eEx \tag{2.19}$$

Using the time dependent part of the Hamiltonian (H'), a perturbation matrix element can be calculated for a given pair of states. This is shown in term 2.20. The index 0 indicates that this is a first order approximation. In a semi-classical description the incident electromagnetic wave would lift an electron from an initial state to another excited state. The transition rate is given by Fermi's Golden Rule, shown in equation 2.21. It is proportional to the square of the dipole matrix element (μ_{if}). [13, 17]

$$H'^0_{if} = eE_0\langle\Psi_i|x|\Psi_f\rangle = E_0\mu_{if} \tag{2.20}$$

$$W_{if} = \frac{\pi|H'^0_{if}|^2}{2\hbar^2}\delta(\Delta\omega) \tag{2.21}$$

As the Hamilton Operator is Hermitian the rate for the reverse transition from the excited state to the initial state is exactly the same as for the transition from the initial to the excited state. [17] Without considera-

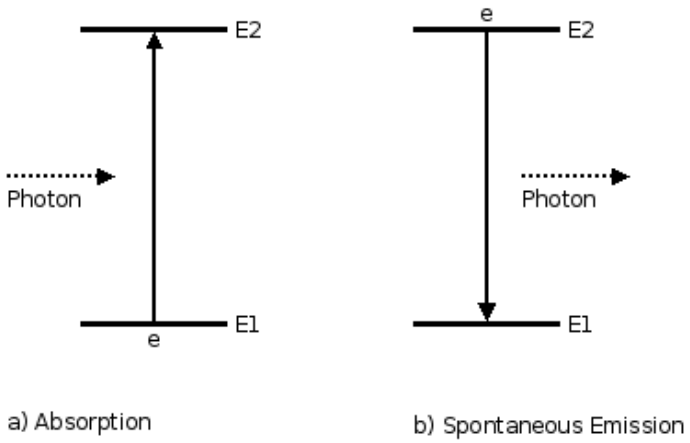

Figure 2.6: Absorption and Spontaneous Emission

tions of lifetimes in certain states or occupation statistics no net emission or absorption would be possible for any electron system. However the reverse transition is not always possible. For example the electron could relax to another energy level. Therefore net rates different from zero for emission and absorption are possible in reality.

2.5.2 Spontaneous Emission and Absorption

Starting from the situation shown in figure 2.6a where energy level E_1 is occupied by one electron, while E_2 is empty, and an incoming photon is resonant to the transition to E_2, the photon will be absorbed and the electron is lifted to the higher energy level. Resonant in this case means that the energy of the photon given by equation 2.17 is equal to the energy difference between the two states. If there is no electron there is of course no likeliness for any interaction between the electromagnetic wave and matter. This process, which destroys photons and lifts electrons to higher states, is well known as absorption. [14, 17]

If the energy of the incident wave is bigger than the bandgap of the material, it will lift an electron to the conduction band by creating a hole in the valence band.

Assuming an electron occupies an excited state (E_2), regardless of how it came there, and if there is an unoccupied electronic state of lower energy (E_1), the electron can descend by emitting a photon. The energy of the photon is again given by the difference between the two state's energies. Figure 2.6b sketches this radiative transition.

Translated from the two level system to real matter, electrons in the conduction band and holes in the valence band can vanish by emitting a photon whose energy corresponds to the bandgap. Momentum conservation leads to a second condition. Emission only takes place in direct semiconductors because only in this case holes and electrons populate the most favorable states with a negligible difference in momentum. [17, 14]

From this point of view absorption and spontaneous emission are similar processes. But there is one important difference concerning the likeliness of the transitions. If all requirements for absorption are met, it will happen with 100% efficiency which means every incident photon will be absorbed. On the other hand the time when spontaneous emission takes place cannot be defined for every electron. It is possible to speak of mean lifetimes in the excited level but for a single electron no accurate statements can be made. [11]

2.5.3 Stimulated Emission

Starting point is again the situation for spontaneous emission, where an electron can be found in the state E_2, while the state E_1 is empty.

An incident photon resonant to the energy difference between the levels E_2 and E_1 is able to produce a second photon by lowering the electron to level E_1. Figure 2.7 illustrates the situation where stimulated emission may take place. The key point is the indistinguishability of these photons. They are identical concerning frequency, phase, polarization and direction. Stimulated emission becomes more likely the more carriers are excited and the more photons reach the electrons in level E_2. [17, 14]

Recalling the statement from section 2.5.1 this doesn't necessarily produce any net emission because the likeliness for emission and absorption is

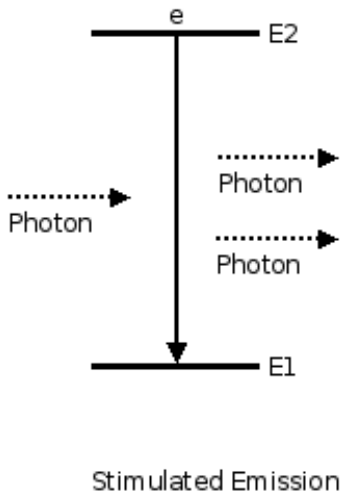

Figure 2.7: Stimulated Emission

the same. As equation 2.22 shows, the photon's balance depends on the occupation statistics of the electron's levels (N_1 and N_2) and on the transition rates for stimulated emission (W_{12}) and absorption (W_{21}). As these transition rates are equal, the photon production rate depends only on the carrier concentrations in the energy levels of interest.

$$\frac{d\rho_{ph}}{dt} = -N_1 W_{12} + N_2 W_{21} = W(N_2 - N_1) \tag{2.22}$$

Spontaneous emission was neglected in this term. By solving this differential equation a function similar to the absorption law is obtained, but the absorption coefficient again depends on the electron's statistics and may become negative. In this case matter changes from absorbing to gain. This solution is shown in equation 2.23 where I(0) can be identified with the incident photon density and I(z) describes the photon density after passing a certain distance in matter. [17, 12]

$$\frac{I(z)}{I(0)} = e^{(N_2 - N_1)\sigma z} \tag{2.23}$$

The character σ is denoted as effective cross section of the atoms. It

depends on the transition rate (W_{12}) and on the intensity of the incident light. [17]

2.6 Intersubband Transitions

Based on the preceding sections the following paragraphs explain transitions of electrons between different states in the conduction band. Starting with emitting and absorbing transitions, also phonon-assisted transitions are explained.

2.6.1 Energy and Momentum Conservation

Electrons that occupy an excited state in the conduction band may descend to lower conduction band levels if there is a free state. These transitions underlie certain criteria. First of all both energy and momentum need to be conserved, expressed in terms 2.24 and 2.25. The indices i and f stand for initial and final state.

$$E_i(\mathbf{k}_i) - E_f(\mathbf{k}_f) = \hbar\omega \tag{2.24}$$

$$\mathbf{k}_i - \mathbf{k}_f \approx 0 \tag{2.25}$$

In bulk material intraband transitions that are only due to emission or absorption of a photon cannot fulfill both conditions because of the relation $E(k) = \frac{\hbar^2 k^2}{2m^*}$. Some momentum changing mechanism such as phonons or traps originating from impurities is needed. [14, 18]

For quantum wells term 2.24 modifies to term 2.26, where ΔE corresponds to the energetic difference of the two subbands. Figure 2.8 describes the emission of a photon due to the transition of an electron between two subbands.

$$E_i(\mathbf{k}_i) - E_f(\mathbf{k}_f) = \Delta E + \frac{\hbar^2 \Delta \mathbf{k}^2}{2m^*} = \hbar\omega \tag{2.26}$$

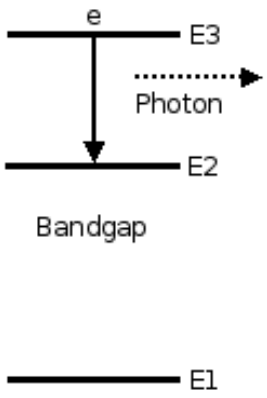

Figure 2.8: Inter-subband Transition

2.6.2 Polarization Selection

The wavefunction of an electron, which is confined in a quantum well in z direction, can be expressed as a product of a slowly varying envelope function (Φ) and a wave part, as shown in term 2.27. In this case Ψ is a function of the three dimensional vector $\mathbf{x}$. The wave part depends on the in-plane momentum ($|k_{\|}| = \sqrt{k_x^2 + k_y^2}$). The envelope function, which is presented in term 2.28, is defined by the width of the quantum well (L) and the order of the state (m).

$$\Psi(\mathbf{r}) = A\Phi_m(z)e^{\iota(k'_x x + k'_y y)} \tag{2.27}$$

$$\Phi_m(z) = \sqrt{\frac{2}{L}}\sin\left(\frac{\pi m z}{L}\right) \qquad m = 1, 2, \ldots \tag{2.28}$$

As mentioned in section 2.5.1 the transition rate can be calculated with Fermi's Golden Rule. It is rewritten in expression 2.29 but instead of the one dimensional coordinate the mid term contains the dot product of the polarization vector (ξ) and the coordinate vector for three dimensions ($\mathbf{x}$). The symbols $\mathbf{k}_{\|}$ and $\mathbf{k}'_{\|}$ stand for the in-plane momentum before and after the transition.

$$\langle \Psi_i, \mathbf{k}_\parallel | \xi \mathbf{x} | \Psi_f, \mathbf{k}'_\parallel \rangle = A \int \Phi_f^*(z) e^{-\iota(k_x x + k_y y)} \tag{2.29}$$

$$(\xi_x x + \xi_y y + \xi_z z)\, \Phi_i(z) e^{\iota(k_x x + k_y y)} dz$$

$$= \xi_z \delta_{\mathbf{k}_\parallel, \mathbf{k}'_\parallel} \int \Phi_f^*(z) z \Phi_i(z) dz \tag{2.30}$$

The terms $\xi_x x$ and $\xi_y y$ are constant with respect to z and therefore can be taken out of the integral, which leads to expression 2.31. The integral over these parts is equal to zero if Φ_i and Φ_f are eigenfunctions of different states because they are orthogonal with respect to each other in this case.

$$\int \Phi_f^*(z) \Phi_i(z) dz = 0 \qquad i \neq f \tag{2.31}$$

Therefore the only part depending on z is is different from zero and the expression for the dipole matrix element can be simplified to term 2.32. In other words transitions between different subbands are only allowed if the polarization of the electromagnetic wave corresponds to the direction of carrier confinement. So QCLs show only gain for light which is TM polarized in relation to the layers of the semiconductor heterostructure. [17, 14]

$$\langle \Psi_i, \mathbf{k}_\parallel | \xi \mathbf{x} | \Psi_f, \mathbf{k}'_\parallel \rangle = \xi_z \delta_{\mathbf{k}_\parallel, \mathbf{k}'_\parallel} \langle \Phi_f | z | \Phi_i \rangle \tag{2.32}$$

When using an abstract two level system the same situation as for interband transitions can occurr. Electrons can be lifted to levels with higher energy by absorbing photons and photons can be emitted in a spontaneous and stimulated way.

2.6.3 Phonons

The position of the atomic cores is not completely fixed in a crystal. At temperatures above 0K lattice vibrations with material-dependent energies exist, named phonons. These vibrations can be classified in two categories, namely acoustic and optical phonons. An infinite string of particles at regular distances can be used as a simple model of a crystal. In a simple approach

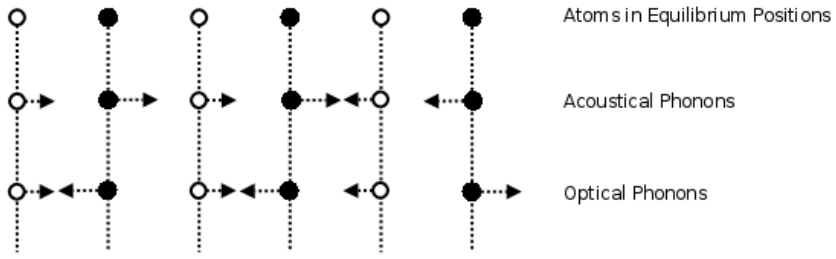

Figure 2.9: Acoustical and optical phonons, after [13]

only forces originating from the nearest neighbor of an atom are taken into account. According to Newton's Law the positions of the atoms can be calculated as solutions to equation 2.33. It has the form of a wave equation and depends on the displacements of an atom (u_i) and it's neighbors ($u_{i\pm1}$), as well as on the atom's mass (M_i) and a coupling coefficient (C). By the use of a dispersion relation allowed solutions to this equation can be found. [13]

$$M_i \frac{d^2 u_i}{dt^2} = C(u_{i-1} + u_{i+1} - 2u_i) \tag{2.33}$$

In figure 2.9 both acoustic and optical phonons are sketched. For acoustic phonons both particles are moved in the same direction whereas optical phonons lead to displacement in opposite directions. As for the following chapters only optical phonons are of interest, acoustic vibrations aren't treated any further.

Phonons are important in semiconductor heterostructures because they allow another type of intraband transitions. Electrons may be lifted to higher energy levels by absorbing a phonon or they may descend to lower states by emitting phonons. Figure 2.10 sketches the phonon assisted relaxation of an electron. The arrow which marks the transition is not vertical in this case because the momentum of the electron changes. The opposite direction of this transition would also be possible. In such a case an electron might be excited by absorbing a phonon.

Since these effects are about one order of magnitude faster than optical transitions, which were described in section 2.5, they can be used to empty certain states or they may be an important parasitic channel which must be

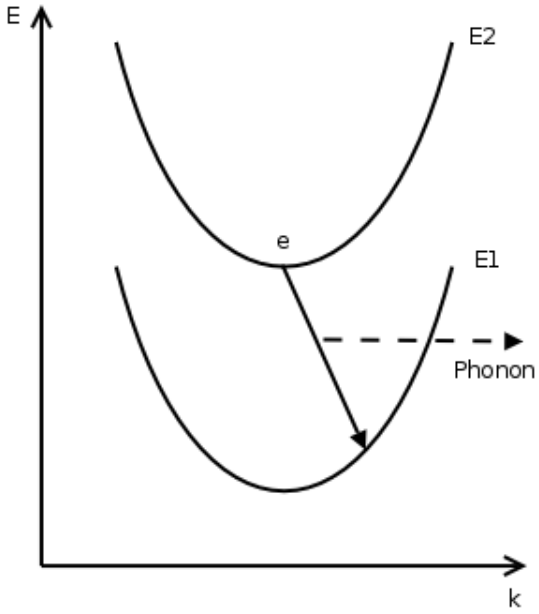

Figure 2.10: Phonon assisted relaxation. An electron can relax from a subband with higher energy (E2) to a subband with lower energy (E1) by emitting a phonon. In k-space this transition is not vertical because parts of the initial momentum of the electron are transferred to the phonon.

included in the model of a device. [13] The energy of longitudinal optical phonons in GaAs is 36meV. [12]

Chapter 3

Theory on Intersubband Lasers

The purpose of this chapter is to discuss the design process of intersubband lasers based on the theory presented in chapter 2. There are four major design families. First QCL operation was demonstrated using 4-well and 3-well designs. [1, 19] Later on QCL performance was improved using bound-to-continuum and superlattice designs. [20, 5, 21] Active regions of 3-well and bound-to-continuum designs are discussed in detail in sections 3.1.1 and 3.1.2.

Here the terms intersubband laser and quantum cascade laser are used synonymously. There is no difference in functionality. When speaking of cascade lasers the potential to grow repetitions of active zones is stressed. In such devices one electron can generate one photon per active region, which allows higher efficiencies and lower threshold currents. Depending on the lattice mismatch large numbers of cascades can be grown. The devices, presented in the next chapters of this work, feature 60 repetitions of the injector and active region structures.

This section will first discuss the 3-well design because of it's simplicity and then concentrate on the bound-to-continuum design because it was used for the experiments presented in this work. Finally other design issues like the geometry of the waveguide and different resonators are described.

3.1 Active Region

Those wells, where the photon emitting transition takes place are named active region. Depending on the number of wells 3-well, 4-well, bound-to-continuum and superlattice designs are distinguished. In superlattice designs up to 8 wells are coupled to produce the energy levels used for lasing.

3.1.1 3-Well-Design

As the name implies there are 3 wells that form the active region. A thin well next to the injector barrier and two thicker wells which are followed by the begin of the next injector structure. As described in section 2.4.1 the thin well contributes an eigenstate with higher energy which acts as upper laser level. The third well empties the lower laser level by the use of resonant LO phonons. Figure 3.1 shows such a design where the upper and lower laser level are labeled as level 3 and 2. The difference in energy between level 2 and 1 are separated by 36 meV which is the energy value for a resonant phonon in GaAs. The electron's lifetime in the upper laser level is around 1.5ps while the lifetime in the lower laser level is only 0.3ps because of the resonant phonon transition. This allows carrier inversion, which is important for lasing operation.[22, 5]

The limited number of states near the lower laser level allows shorter wavelengths as a higher energy difference can be used for the lasing transition. [22]

3.1.2 Bound-to-Continuum Design

The bound-to-continuum design takes advantage of an additional well added to the active region. Thinner barriers between the thicker wells of the active region result in stronger coupling between these wells. A quasi continuum is formed below the lower laser level because of the additional states. Similar to the 3-well design the upper laser level is a bound state of a thin well next to the injector barrier. [22]

Figure 3.2 shows the conduction band edge profile of sample H149 which

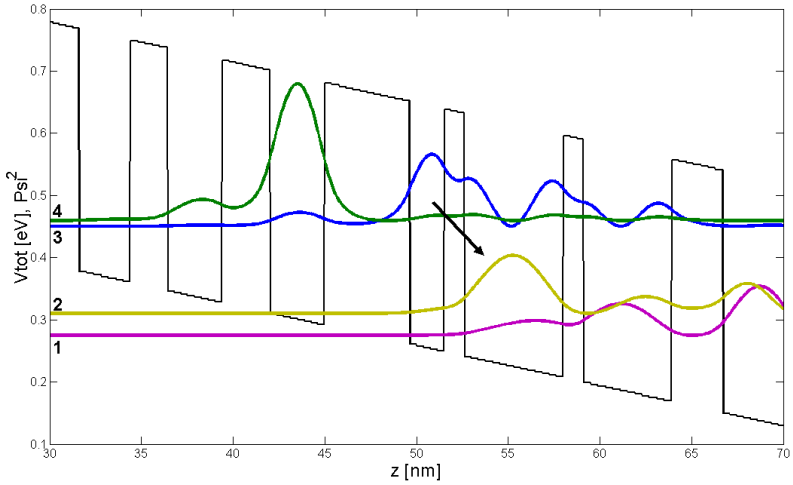

Figure 3.1: Conduction band edge profile of a 3-well design, after [22]. The injector ground state is labeled as level 4. Levels 3 and 2 act as upper and lower laser level. The difference between levels 2 and 1 corresponds to the energy of a LO-phonon, which allows efficient depletion of level 2.

was used for the experiments presented in the following chapters. The upper and lower laser level are labeled 3 and 2 in the plot. Compared to the structure shown in figure 3.1 more levels below level 2 can be found. The arrow marks the lasing transition, which corresponds to an energy of 127.9meV or 9.70 μm, at an applied electric field of 48kV/cm.

The plenty of states below the lower laser level lead to a better carrier extraction from the active region. This is because electrons can tunnel from all of these delocalized states directly into the injector states of the next cascade. Although the lifetime of the lower laser level is more or less the same for these two designs, the 3-well design has a higher effective lifetime because coupling with the injector states is not as efficient. [23]

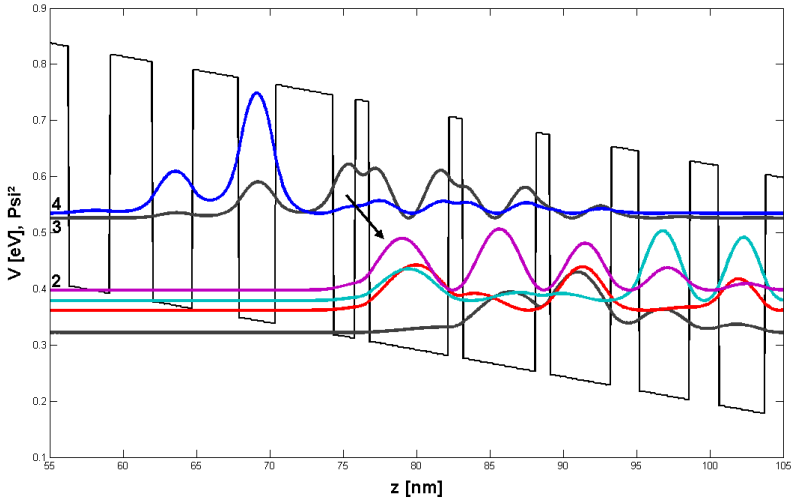

Figure 3.2: Conduction band edge profile of a bound-to-continuum design. The complete structure is shown in table 4.1.3. Additional states below level 2 form a quasi continuum, which allows efficient depletion of the lower laser level.

3.2 Injector Region

In order to inject electrons into the upper laser level or extract them from the lowest level of the active region chirped superlattice structures are used. This structure must provide many delocalized states at the end where carriers are extracted from the active zone and at least one state that enables an efficient transition rate to the upper laser level.

Because there are many quantum wells with small variations in well width a high number of energy levels is formed very close to each other in terms of energy. Although these are discrete states this phenomenon is often called the formation of a miniband.

3.3 Inversion

In section 2.5.1 a term for the probability of optical transitions was given. But as this term is equal for spontaneous emission and absorption no change

in the photon balance should occur. The key to allow light emission from these two level systems is population inversion.

It is very important to empty the lower laser level and fill the higher laser level at high rates. In this case absorption can't happen because no electrons populate the lower laser level and therefore cannot be absorbed resonantly to the higher laser level. In other words the lifetime of carriers in the upper laser level should be rather big while the carriers should relax as fast as possible from the lower laser level to other states.

$$G = \sigma \Delta n = \sigma \frac{J}{q_0} \left[\tau_3 \eta_3 \left(1 - \frac{\tau_2}{\tau_{32}} \right) - \eta_2 \tau_2 \right] \tag{3.1}$$

Equation 3.1 allows to estimate the gain of a quantum cascade laser. Basically it depends on the population inversion in the two laser levels. The constant σ is called the transition cross-section and is proportional to the dipole matrix element and inversely proportional to the width of the electroluminescence peak. The factors η_3 and η_2 allow to include the parasitic relaxation of carriers from the injector to the lower laser level ($\eta_2 \tau_2$). In order to achieve high gain an optimal combination of population inversion and the dipole matrix element must be found. [22, 20, 23]

Population inversion does not only depend on the conduction band structure as mentioned above, but also on pumping. The relation between current and power for the devices of H149I B1 is shown in figure 3.3. For small current densities carriers relax to the lower levels by spontaneous emission or other non-radiative paths. At a certain value of the pumping current waveguide losses are overcome by stimulated emission and the semiconductor material changes from absorption to gain. After this so called threshold current the optical output power increases with a large gradient.

When operating at higher temperatures thermally excited carriers are able to jump over barriers or change to states of higher energy. Also phonon related transitions become more favorable. Therefore the percentage of carriers that populate the lower laser level instead of relaxed levels beneath raises. As a consequence of this the carrier inversion term in equation 3.1 is reduced. To be less sensitive to this behavior the bound-to-continuum design

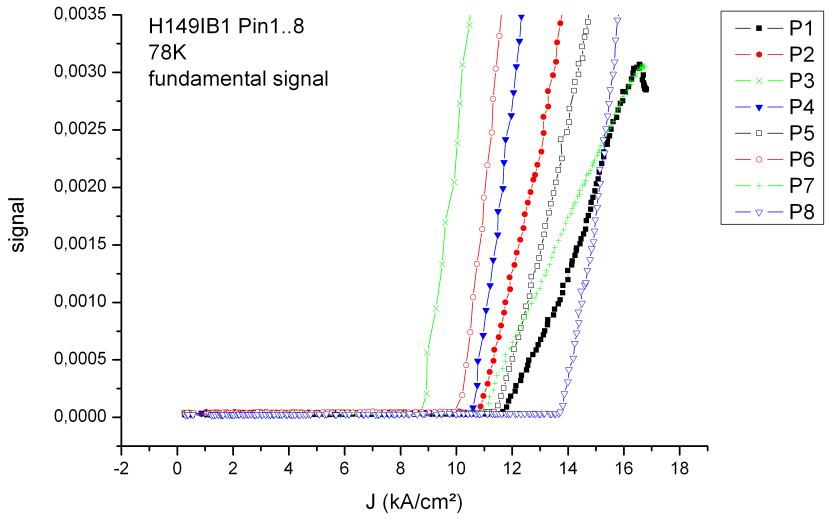

Figure 3.3: Current Density - Optical Power Relations for samples of structure H149, as shown in table 4.1.3, with phasematch gratings. All devices have a length of 2mm and a width of 30 μm. These characteristics were measured in pulsed mode with a pulse length of 100ns and a repetition rate of 5kHz at a temperature of 78K.

offers more states below the lower laser level to allow efficient depletion.

3.4 Waveguide

Section 2.5 denoted that photons and electromagnetic waves are dual descriptions of the same phenomenon. Because the rate of stimulated emission depends on the number of incident photons it is necessary to confine the light in some kind of waveguide structure in order to reduce the threshold current density and to improve the optical gain. The area with the highest electromagnetic intensity should overlap with the active region where stimulated emission takes place. The following sections show concepts to achieve confinement of the electromagnetic waves.

In figure 3.4 the basic geometry of a QCL processed in a waveguide struc-

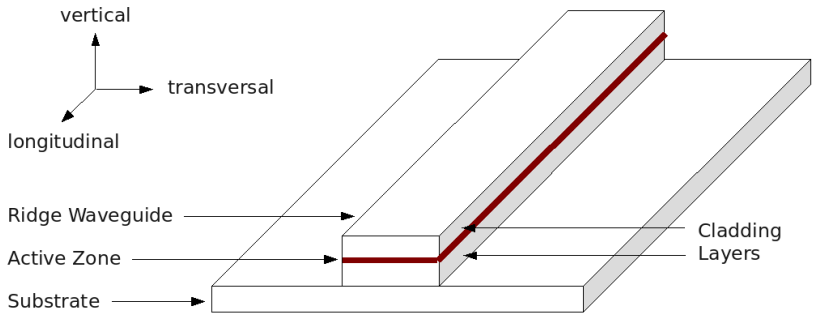

Figure 3.4: Ridge Waveguide

ture is shown. Also the directions for mode confinement are labeled.

3.4.1 Reflectivity and Transmissibility

When discussing propatagion of electromagnetic waves, every material is characterized by it's refractive index. Disregarding sections with infinite conductance, only finite refractive indices occur. As a consequence of this the discontinuity of the refractive index at a general interface can only be finite.

Electromagnetic waves, which hit an interface, are split into a reflected and a transmitted part. The in-plane parts of the wavevectors of incident, reflected and transmitted wave parts must be identical, as expressed in term 3.2.

$$k_{\parallel,i} = k_{\parallel,r} = k_{\parallel,t} \tag{3.2}$$

As a second condition, the wavevectors must fulfill the dispersion relation for correspondent material, which is presented in expression 3.3.

$$|k_{i,r,t}| = n_{i,r,t} k_0 \tag{3.3}$$

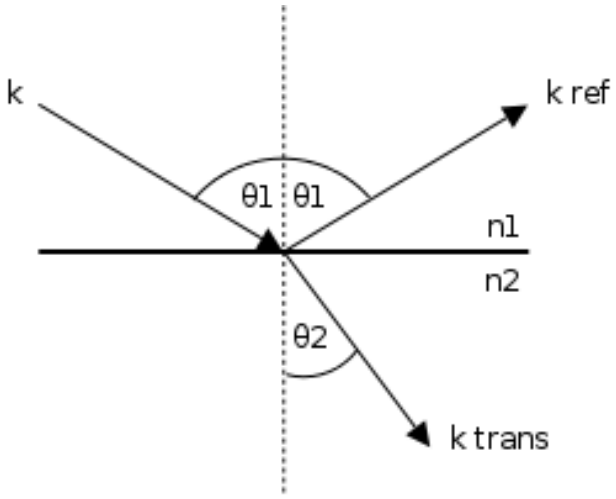

Figure 3.5: Refraction of an electromagnetic wave at an interface between materials with different refractive indices. One part of the incoming wave is reflected under the same angle as the incident wave, while the other part is transmitted under an angle, which depends on the ratio of the refractive indices.

These two constraints lead to expressions 3.4 and 3.5, which allow to calculate the amplitude coefficients for the reflected and transmitted parts of the wave. These are only valid for TM polarized light, which means that the magnetic field vector lies coplanar to the interface. Figure 3.5 shows the according geometry of the wavevectors. One part of the wave is reflected under the angle of the incident light (θ_1), while the other part is transmitted under an angle, which depends on the ratio of the refractive indices (θ_2). [17]

$$r_\pi = \frac{n_2 \cos(\theta_1) - n_1 \cos(\theta_2)}{n_2 \cos(\theta_1) + n_1 \cos(\theta_2)} \tag{3.4}$$

$$t_\pi = \frac{2n_1 \cos(\theta_1)}{n_2 \cos(\theta_1) + n_1 \cos(\theta_2)} \tag{3.5}$$

The refractive indices (n_1 and n_2) of the materials used for the QCLs, presented in this work, are summarized in table 3.4.1. Due to dispersion these

material parameters are changing with the wavelength of the light. Therefore values for the wavelength regions of fundamental and second harmonic signals are given.[17]

Material	**N_d (cm^{-3})**	**n (10.5μm)**	**n(5.2μm)**
GaAs	4e16	3.26 [24]	3.30 [24]
GaAs	4e18	2.20 [24]	3.08 [24]
$Al_{0.9}Ga_{0.1}As$		2.81 [24]	2.86 [24]
H149 Active Zone		3.21	3.24
Si_3N_4		1.25[25]	2[25]

Table 3.1: Refractive indices at $5\mu m$ and $10\mu m$. The Drude Model for free carrier absorption is included.

When electromagnetic waves propagate from a material with higher optical density to another one with lower refractive index, there is a certain angle for every combination of the refractive indices from where no light is transmitted. The critical angle for this total reflectance can be calculated by equation 3.6.

$$\Theta_{crit} = \arcsin\left(\frac{n_2}{n_1}\right) \tag{3.6}$$

For angles larger than this critical angle there are no propagating waves in material 2, although there are evanescent fields that can be used for waveguide coupling. [17]

3.4.2 Vertical Confinement

The $GaAs/Al_xGa_{1-x}As$ material system doesn't provide the advantage of the natural waveguide in vertical direction, known from lasers on InP substrates. Unfortunately GaAs has a higher refractive index than AlAs and therefore the electromagnetic mode would be attracted by the substrate. This is undesirable because the region with the highest radiation intensity should overlap with the region of gain to enable lasing.

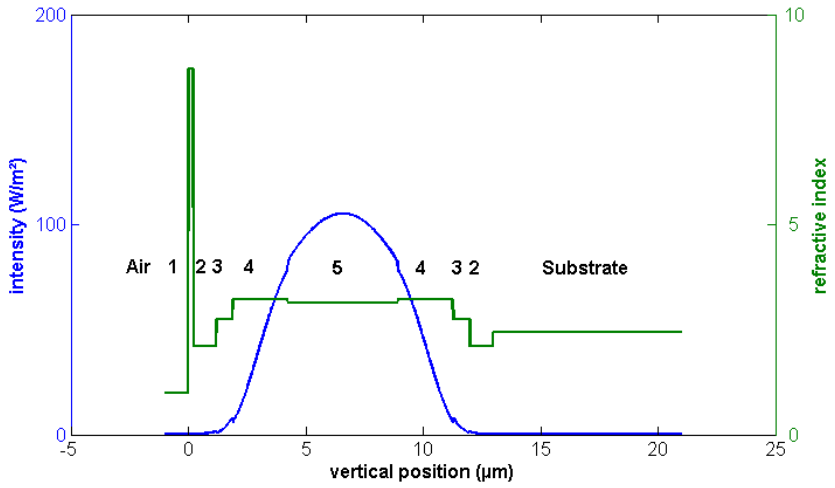

Figure 3.6: Vertical mode profile in H149. The active region (5) is surrounded by waveguide core layers (4) consisting of GaAs. These are followed by $Al_{0.9}Ga_{0.1}As$ layers (3) and low doped GaAs cladding layers (2). On top of the structure there is a gold layer (1). The intensity of the light is confined around the active region of the semiconductor heterostructure.

Some efforts are necessary to confine the mode in the waveguide structure containing the cascade of active regions. Usually the superlattice structure is embedded between GaAs and AlAs layers. The boundary layer in between acts as a reflective interface.

Figure 3.6 shows the distribution of the Poynting Vector across the layer profile of sample H149. A detailed description of this layer sequence is shown in table 4.1.3. The peak of the refractive index at a vertical position of $0\mu m$ corresponds to the gold layer acting as top contact. Highly doped GaAs cladding layers labeled as layer 2 in the figure provide a good contrast of the refractive index compared to the active region around $6\mu m$. Therefore the electromagnetic field is confined within the active region.

3.4.3 Lateral Confinement

In comparison to the vertical direction, lateral confinement is rather easy to achieve. Usually QCLs are processed as ridge waveguides delimited by deep etched trenches. Also they are coated with a passivation layer consisting of Si_3N_4 that provides total reflectance for angles over 37° .

3.5 Resonators

Resonators are necessary to confine the light in longitudinal direction. At these interfaces the incident light has an angle of nearly 0° , so this problem can't be solved by total reflectance. The following sections show the two most popular approaches and their influence on the spectrum of the emitted light.

3.5.1 Fabry Perot Resonators

Parallel mirrors, forming a cavity, are called Fabry Perot resonators. In most cases the cleaved edges of the laser structure are used as mirrors. The reflectivity can be calculated using equation 3.7 from the difference of the refractive indices of the waveguide (n_1) and the medium outside the waveguide (n_2). For GaAs and vacuum or air a reflectivity of about 0.3 can be achieved. [17]

$$R = \left(\frac{n_1 - n_2}{n_1 + n_2}\right)^2 \tag{3.7}$$

Constructive interference and therefore gain is possible for all longitudinal modes, whose wavelength (λ_m) fulfills equation 3.8. The symbol m is the index of the mode, which corresponds to the number of roots along the waveguide. Furthermore L is the length of the resonator and n matches the refractive index of the waveguide material. [17]

$$\lambda_m = \frac{2nL}{m} \tag{3.8}$$

The typical length of a Fabry Perot cavity is in the region of a few millime-

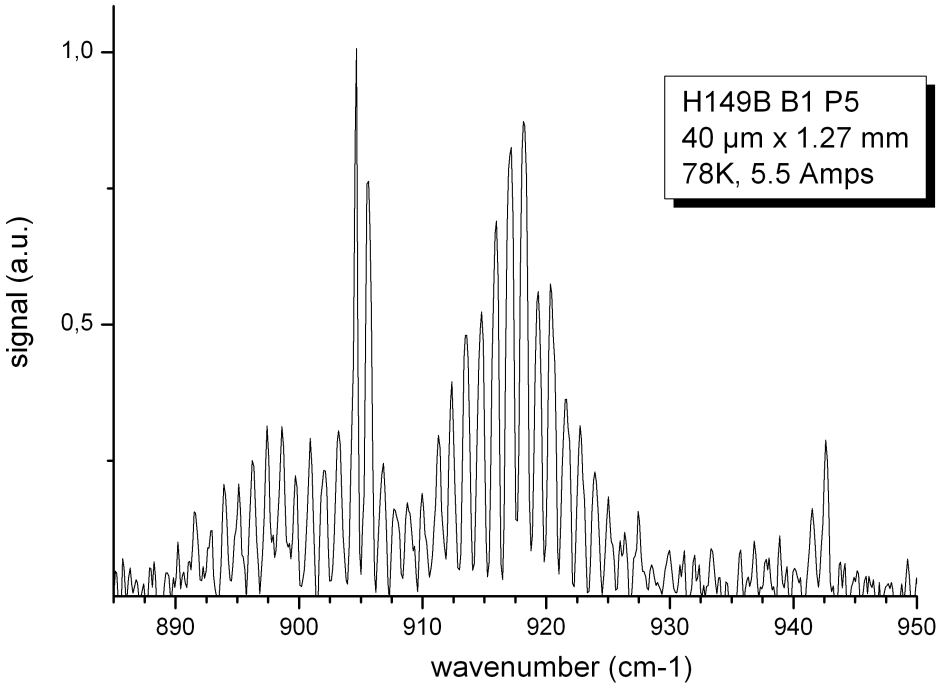

Figure 3.7: Fabry Perot Spectrum (H149, 78K)

ters. As this is much longer than the emitted wavelength many longitudal modes can oscillate in the cavity. This leads to a broad emission spectrum which is limited by the wavelength dependence of the optical gain. Figure 3.7 shows a typical Fabry Perot spectrum. The modes are equally spaced in a scale of wavenumbers. For a length of 1.27mm and a refractive index of 3.21, as presented in table 3.1, one calculates one peak per 1.2/cm, which is in good agreement with the plot.

3.5.2 Distributed Feedback Grating

With formula 3.7 it is possible to calculate the reflectivity at any interface that shows a contrast concerning the reflective indices. Such interfaces can be arranged in a way that the partially reflected waves of all interfaces inter-

fere constructively. The reflectivity of such a distributed feedback mirror is given by term 3.9, where m denotes the number of layer pairs consisting of a material with higher and another one with lower refractive index. [17]

$$R = \frac{1 - \left(\frac{n_l}{n_h}\right)^{2m}}{1 + \left(\frac{n_l}{n_h}\right)^{2m}} \tag{3.9}$$

The reflectivity is best, when the wave is in resonance with the bragg wavelength of the mirror structure, which can be calculated with equation 3.10. [26] The layer period Λ and the effective refractive index of the waveguide n_{eff} define the optical length of one period. Furthermore the symbol M describes the order of the grating.

$$\lambda_B = \frac{2n_{eff}\Lambda}{M} \tag{3.10}$$

These periodic layer structures are realized by etching a surface grating into the ridge waveguide of the QCL. Figure 3.8 shows a ridge waveguide QCL with a DFB grating on top of the waveguide. Because the reflection coefficient depends on the wavelength, distributed feedback gratings lead to narrow gain bandwidths. These resonators can be used for single mode emission. [27, 28]

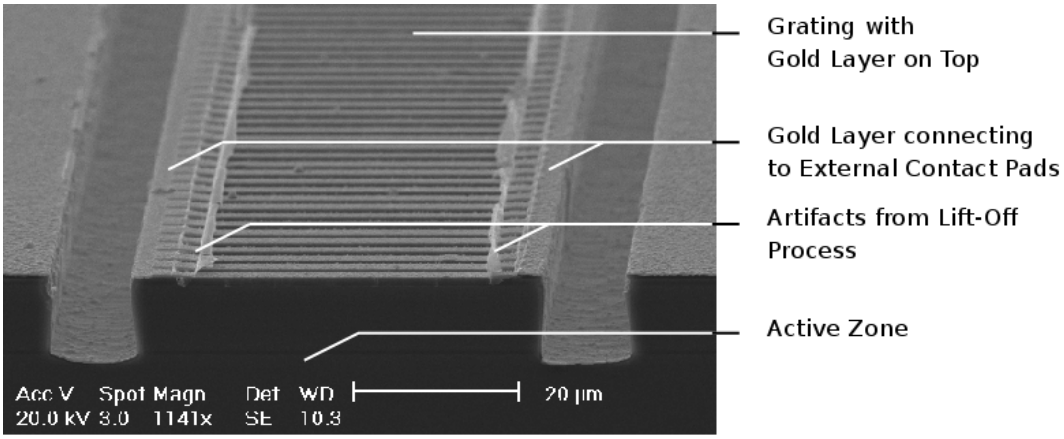

Figure 3.8: Ridge waveguide with 4^{th} order DFB grating. The grating has a period of 3.44 μm. First the top contact on the grating was formed by evaporation. Then the ridge structure was covered with another layer of gold, which connects the laser device with external contact pads. To allow surface emission, the topmost gold layer was removed from the upside of the ridges. Artifacts of this lift-off process can be seen near both sidewalls of the ridge.

Chapter 4

Fabrication and Measurement Setups

Taking the devices whose data are presented in this thesis as example, the essential processing steps that are necessary to fabricate QCLs are explained. Hence this shall not be a complete overview on semiconductor processing techniques.

4.1 Growth of Semiconductor Heterostructures

This section describes the bottom-up part of QCL fabrication. Although the first theoretic proposal was published in 1971, it took until 1994 to fabricate the first QCL. [29, 19] Today two different techniques are used for the growth of semiconductor heterostructures. Molecular beam epitaxy (MBE) is used, where the control over the thickness of the layers is critical. The alternative is metal-organic chemical vapor deposition (MOCVD), which allows higher growth rates but only for certain materials. Also the quality of structures that are grown by MBE can not be reached. The thickness of the layers can not be controlled as precise and defect densities are higher.

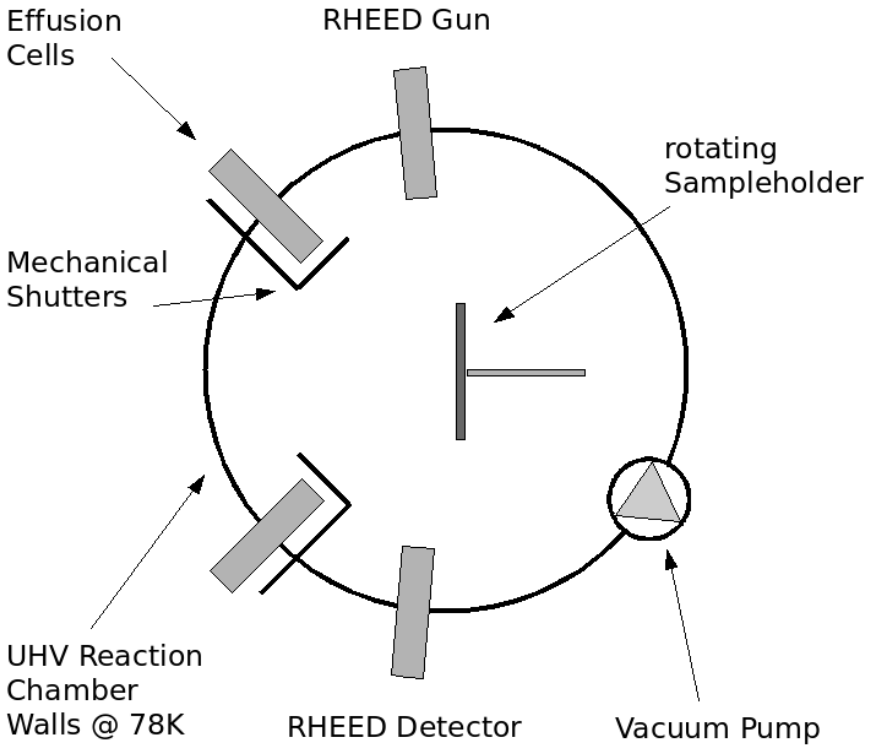

Figure 4.1: MBE Facility

4.1.1 Molecular Beam Epitaxy

As mentioned above MBE is used, wherever layers with highest possible uniformity and as few as possible impurities are necessary. In semiconductor heterostructures these quality factors lead to a high carrier mobility and to good control of the energy levels.

The working principle of MBE is simple. A substrate wafer is exposed to molecular beams of the desired elements, which crystalize at the surface of the substrate. The temperature of the substrate must be controlled precisely to allow motion across the surface on one hand and to prevent thermal induced desorption on the other hand. The term molecular beam only applies to situations where the mean free path of a particle is bigger than the distance between the particle's source and the target. [30]

For an ideal gas the mean free path (L) can be calculated with equation

4.1. It is inversely proportional to the square root of the molecule's concentration (n) and their diameter (d). In typical MBE facilities the distance between effusion cell and substrate is about 20cm, which means the mean free path of the molecules should be larger than this value. Therefore this equation can also be used to get a maximum concentration of molecules.

$$L = \frac{1}{\sqrt{2}\pi n d^2} \tag{4.1}$$

This concentration can be transformed into a pressure with the help of the ideal gas law, shown in equation 4.2.

$$n = \frac{p}{k_B T} \tag{4.2}$$

Assuming a distance of 20cm and room temperature (273K) the pressure in the reaction chamber of the MBE should be less than 7.7e-2Pa. This however is not the limiting factor. In order to reduce impurities originating from the residual gas in the reaction chamber the base pressure should in the ultra high vacuum range, which lies below 1e-6Pa. Typical pressures during growth are in the range of 1e-5Pa. [30]

The source materials are vaporized in so called effusion or Knudsen cells. Bulk material is placed inside a heated chamber with an small orifice, pointing to the substrate holder in the reaction chamber. Effusion rate and therefore growth speed is proportional to the cell temperature. The molecular beam can be directed to the sample or it can be blocked by a mechanical shutter. [30]

4.1.2 RHEED

The principles of the basic MBE process, explained in section 4.1.1 are quite simple. Nevertheless in reality this is one of the most complicated steps in semiconductor fabrication. Growth parameters like the temperature of the effusion cells or the opening and closing of the shutters need to be controlled accurately. In particular feedback on the surface morphology and growth rates is needed.

This can be done by reflection high energy electron diffraction (RHEED). Almost every MBE is equipped with this instrumentation. A beam of electrons that have energies in the range of 5-40keV, depending on the material to be investigated, is targeted at the sample under a grazing angle (1-3°). Because of the short de Broglie wavelength of these electrons interaction between the electron beam and the sample only takes place in the topmost atomic layers. After hitting the sample surface the beam is reflected to a phosphorescent screen, which shows a projection of the reciprocal lattice. [30]

Changes of the surface structure cause a change of the diffraction pattern in the RHEED detector. Growing leads to oscillations of the intensity, which allow to count the number of deposited atomic layers on the substrate.

4.1.3 Growth of H149

The layers of the active region and the waveguide were grown in a solid source Intervac Gen II molecular beam epitaxy system. The exact sequence of layers is given in table 4.1.

There are two nested loops which produce a total of 60 active regions and 64 injector regions. After every 15 active regions a doped spacer layer is inserted. This should enable heat transport to the sidewalls of the structure.

In order to get good electric contacts a highly doped $In_{0.5}Ga_{0.5}As$ layer is grown on top of the structure. Compared to the GaAs layers the carrier concentration can be increased by two orders of magnitude.

4.2 Etching of Grating and Ridge Waveguide

This section describes the structuring of the gratings and the ridge waveguide. The transfer of the etch mask structure to the sample was done by means of conventional optical lithography. A layer of positive photoresist was exposed to UV light under a chromium mask and then developed with an organic base. This structure was then used as etch mask.

Since all device structures that are discussed here were done with dry

etching processes using a PlasmaLab 100 facility, these technique is explained in the next sections.

4.2.1 Reactive Ion Etching

Reactive ion etching (RIE) is a dry etching technique, which can be used to remove material in an anisotropic way. The etchants are reactive by itself and are additionally accelerated towards the sample, so it can be described as kinetically assisted chemical etching.

Because the process gases are reactive this process is not only anisotropic but also shows weak isotropic behavior, which should be low compared to the directional part. Figure 4.2 sketches a RIE facility. The sample is placed in a reaction chamber, which is first evacuated and then filled with reactive gases. Typical pressures during the process are in the range of several hundred pascals. Lower pressures lead to better directionality due to the reduced scattering of the etchant molecules, but at reduced etch rates. A radio frequency (RF) electric field then ignites a plasma, which activates the etching process. One electrode is the sample holder, while the second one is the reaction chamber itself. [31]

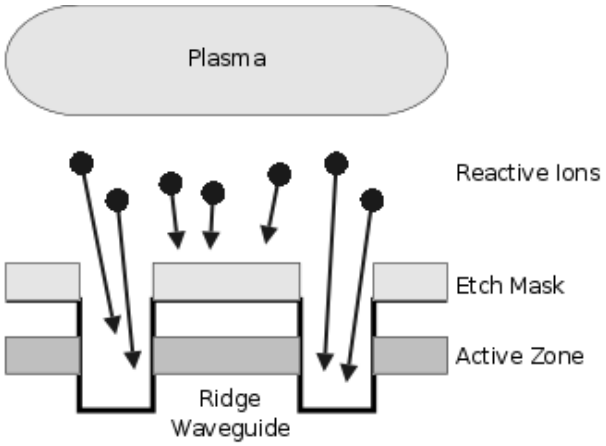

Figure 4.2: Etching of Ridge Waveguide Structure with RIE

The main two advantages of this process are the anisotropic behavior,

which can be used to create deep trenches or holes and the good process control. When reaching the desired etch depth, the process can be stopped by turning the RF field off. [31]

4.2.2 Interferometric Endpoint Detection

The etch depth can be measured in-situ by the use of an interferometer. Coherent light is sent to the sample surface, depending on where it hits the surface it is reflected into a detector from either the etch mask or directly from the sample. During the process the distance between etch mask and sample surface increases, wich causes oscillations in the detected signal.

The height difference (d) for one oscillation of the light can be calculated by equation 4.3, where λ is the wavelength of the laser used in the interferometer. [17]

$$\Delta d = \frac{\lambda}{2} \tag{4.3}$$

4.2.3 Waveguide with Phase Match Grating

The waveguides of the QCLs discussed in the following chapter were were fabricated with two subsequent etch processes. In both cases $SiCl_4$ was used as etchant. First the grating structures were etched to a depth of 1 μm. In the next step trenches, which provide lateral confinement of the electromagnetic modes were etched. They must be etched considerably deeper than the active zone of the QCL. In this case the etch process was stopped at a depth of 10 μm.

4.3 Passivation Layer

In order to avoid short circuits at the sidewalls of the laser ridges a layer of Si_3N_4 was deposited on the surface of the sample. This is done by another plasma assisted process, called plasma enhanced chemical vapor deposition

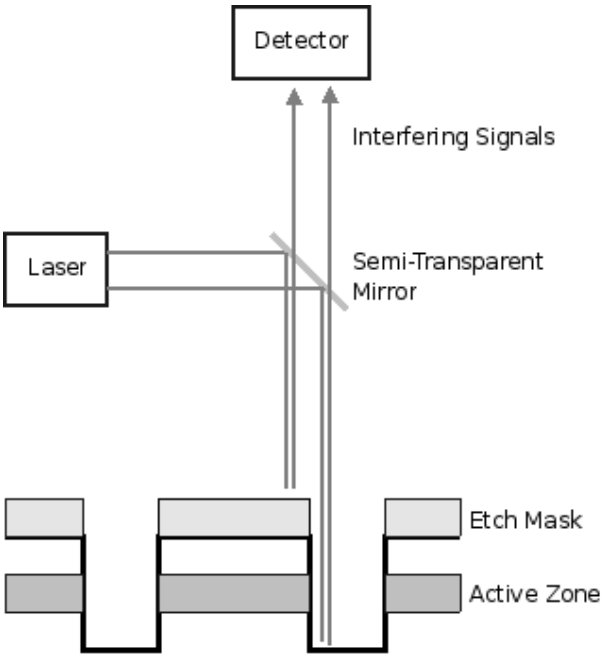

Figure 4.3: Interferometric Endpoint Detection

(PECVD). The PECVD facility is somewhat similar to the RIE facility. Basically it is a reaction chamber where the precursor gases can be mixed at different ratios and at given pressures, typically 15Pa and above. Two RF driven electrodes allow to ignite a plasma in the chamber. The sample is placed on a surface, which can be hold at 300-400°C . [31]

The basic chemical reaction is shown below in equation 4.4. The precursor gases are cracked at the heated sample surface, which produces a layer consisting mainly of Si_3N_4. Depending on the process parameters, layers of differing compositions can be deposited. The hydrogen content can be up to 25%. Lower temperatures lead to a higher content of H_2, which results in a lower refractive index. [31]

$$3\ SiH_4 + 4\ NH_3 \rightarrow Si_3N_4 + 12\ H_2 \tag{4.4}$$

With the use of an Oxford Systems PlasmaLab 80 plus facility a 300nm thick layer of Si_3N_4 was deposited on the samples. As depicted in figure 4.4

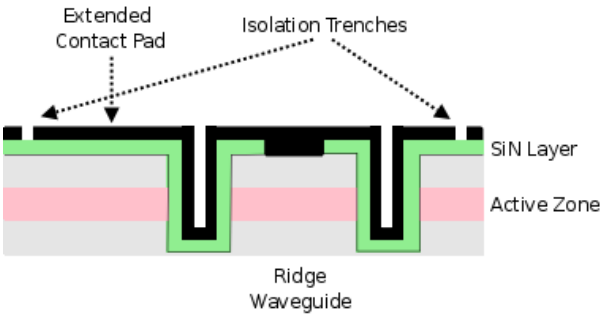

Figure 4.4: Si_3N_4 Passivation Layer and Top Contact

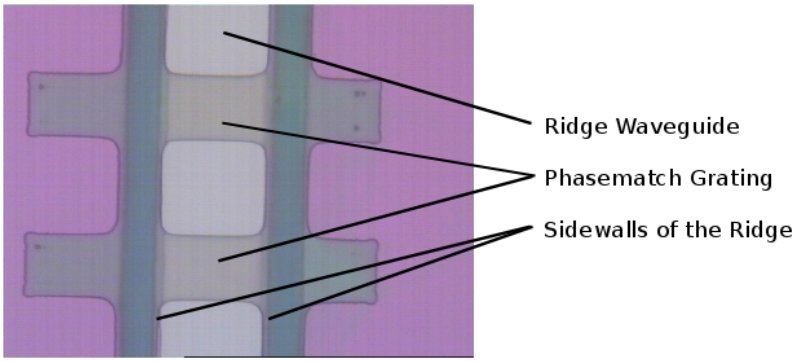

Figure 4.5: Photo of a ridge waveguide with phase-match grating and Si_3N_4 passivation layer

the silicon nitride film provides electric insulation at the sidewalls of the laser ridges.

To make electrical contacting possible, the passivation layer was opened on top of the ridges. This was done with the PlasmaLab 100 facility using SF_6 as etchant. A detail of a laser ridge prepared for deposition of the metallic layer on top is shown in figure 4.5.

4.4 Electrical Contacts

The metallic contact layers on top of the devices were created with a sputter system. The term sputtering applies to plasma assisted processes where ions

of an inert gas are accelerated towards bulk targets of the desired element. Atoms are torn out of the target and coat the surface of the samples uniformly. For the processing of the H149 samples an Ardenne LS320S sputter system was used. Compared to the MBE process the pressure in the reaction chamber is much higher, which causes the target atoms to coat all surfaces without showing a preferred direction. [32]

To provide electric insulation, thin stripes of photoresist were fabricated by optical lithography. In the next step the surface was covered with a thin layer of Titanium, which acts as an adhesive agent for the following gold layer. The later one had a thickness of 1 μm. It's purpose is to provide metallic contacts with extended contact pads on top of the devices. Finally the devices were separated by lifting off the photoresist stripes with metal on top. Figure 4.4 shows the final structure of the QCL devices.

4.5 Mounting and Bonding

In a final fabrication step all samples were soldered on copper plates, which are used as common back contact of the devices and as heat sinks. Indium was chosen as soldering agent because it allows a good thermal contact to copper.

Electric contacting was done by gold wires with a diameter of 25 μm. The copper plate with the semiconductor devices soldered was heated to 125°C . Then the gold wires were bonded using a wirebonder which applies a force of 0.147N and ultrasonic. The resulting configuration is sketched in figure 4.6.

4.6 Measurement Setup

The following sections show the setups that were used to characterize the devices fabricated from the material H149. For all experiments the samples were placed in a cryostat that can be cooled with liquid nitrogen or helium.

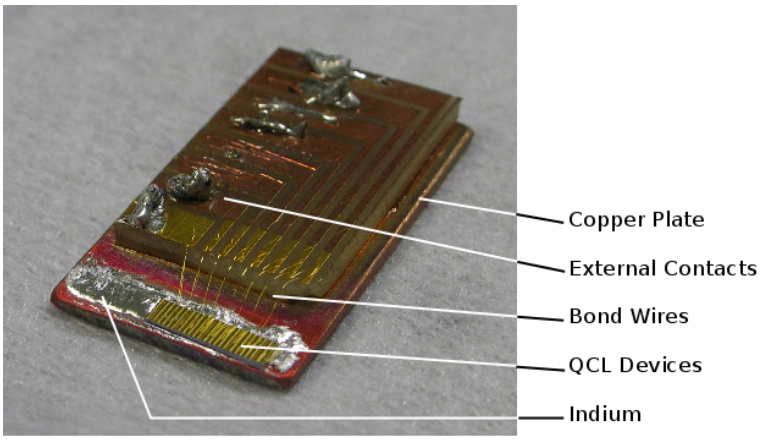

Figure 4.6: Mounting of QCL devices. The indium layer provides good electrical and thermal conducttance to the copper plate, which acts as a common back contact of the devices.

4.6.1 Detectors

Light with wavelengths around 10 μm was measured using a deuterated triglycine sulfate (DTGS) detector and a mercury cadmium telluride (MCT) detector. Second harmonic signals were quantified by the use of an InSb detector. The following paragraphs summarize the working principles and characteristics of these detectors.

Triglycine sulfate (TGS) detectors rely on the pyroelectric effect. Inciding electromagnetic waves are absorbed in the detector element, which leads to a temperature shift. As a consequence of this the spontaneous polarization state changes and can be measured as a voltage change. Usually these detectors feature an integrated field effect transistor to make the detector characteristics independent from the electric circuit. The spectral response of pyroelectric detectors itself does not depend on the wavelength, however in reality it is limited by the window material. [33, 34]

MCT detectors belong to the group of photoconductive detectors. Electromagnetic radiation leads to an increase in conductivity. The ternary alloy $Hg_xCd_{1-x}Te$ has a direct bandgap which can be adjusted by varying the material's composition. The wavelengths that can be absorbed in a range from 0.7

to 25 μm. Absorbed photons create electron hole pairs that can be detected by a readout circuit, which applies a bias voltage. The main drawback of these detectors is the need of liquid nitrogen cooling. [35] Figure 4.7a shows the spectral response for several MCT detectors. Devices which are used for wavelengths around 10 μm also show responsivity for the second harmonic signal near 5 μm but at much lower sensitivities.

In this work an InSb photodiode was used to detect light with wavelengths around 5 μm. Detectivity as a function of wavelength is sketched in figure 4.7b. Although these devices could be used at room temperature they were cooled with liquid nitrogen, which increases the sensitivity by two orders of magnitude. The InSb diode was directly connected to the current input channel of the lock-in amplifier. [36, 33]

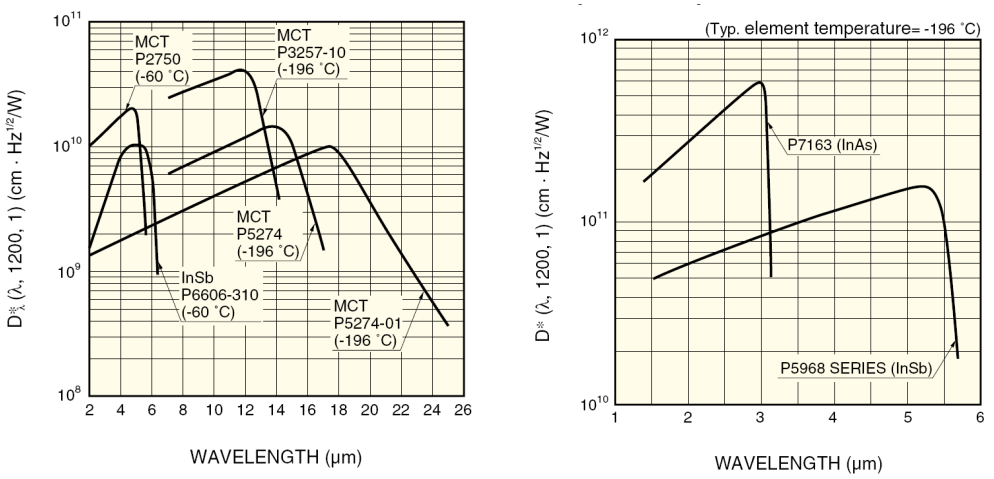

a) b)

Figure 4.7: Detectivities for MCT and InSb Detectors, from [34]

4.6.2 Pulse Generator and Measuring Instruments

The QCLs were powered with an AVTech AVL-2-B transmission line pulser, which was operated at a repetition rate of 5kHz. A Tektronix TDS 3032B oscilloscope with a current probe was used to measure the current supplied.

Optical power was determined with the use of a lock-in amplifier by EG&S Princeton Applied Research (5210). The lock-in amplifier demodulates all signal components that oscillate with the frequency of the pulse generator. Thermal noise is masked out by this technique, which allows to quantify signal parts that are below the noise level. [37]

4.6.3 Optical Path

The devices to be measured were mounted in a cryostat with ZnSe windows that had an antireflective coating for wavelengths of 10 μm. A ZnSe lens with a diameter of 1.5" and a focal length of 1.5" was used to get a collinear beam which was then guided through the FTIR. Then the optical signal was guided to the appropriate detector. In the case of the InSb detector which was used for signals in the range around 5 μm the signal was focused with a parabolic mirror, which had a focal length of 17.8 cm.

When measuring current - power relations or spectra, the setup sketched in figure 4.8 was used. The signal path which was used to measure the power of the fundamental mode was perpendicular to the facet which acts as fabry perot mirror. In the case of second harmonic measurements, the lasers were tilted by an angle of 30° . This modification to the setup was necessary to detect parts of the farfield, which showed high intensities of the second harmonic signal. This will be discussed accurately in the next chapter.

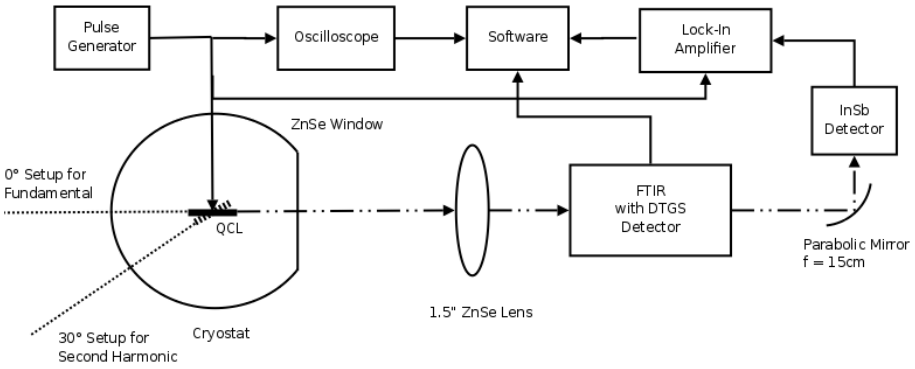

Figure 4.8: Measurement setup for spectral characterization and current-power relation measurements

Layer				Al content (%)	Thickness (Å)	Doping (Si)
n+ GaAs Substrate					350 ± 20 μm	2e18
GaAs					10000	4e18
AlGaAs				90	7000	1.5e17
GaAs					23500	4e16
Loop 1 (4x)	**Loop 2** (15x)	**Injector**	AlGaAs	48.7	38.4	
			GaAs		25.7	
			AlGaAs	48.7	30.9	
			GaAs		27.4	2.5e17
			AlGaAs	48.7	29.1	1.3e17
			GaAs		28.3	2.5e17
			AlGaAs	48.7	27.2	1.3e17
			GaAs		28.3	2.5e17
			AlGaAs	48.7	23.4	1.3e17
			GaAs		28.3	2.5e17
			AlGaAs	48.7	21.6	
			GaAs		29.2	
			AlGaAs	48.7	21.6	
			GaAs		30.1	
			AlGaAs	48.7	19.7	
			GaAs		31.9	
			AlGaAs	48.7	19.7	
		Active Region	GaAs		34.5	
			AlGaAs	48.7	18.8	
			GaAs		42.5	
			AlGaAs	48.7	9.4	
			GaAs		49.6	
			AlGaAs	48.7	9.4	
			GaAs		54.0	
			AlGaAs	48.7	9.4	
			GaAs		15.9	
	Additional Injector					
	GaAs				1500	4e16
GaAs					22000	4e16
AlGaAs				90	7000	1.5e17
GaAs					10000	4e18
InGaAs (50% In)					50	2e19

Table 4.1: H149 Layer Sequence

Chapter 5

Second Harmonic Generation

So far all chapters presented the basic functionality in QCLs that can be explained within a linear theory. In consideration of nonlinear effects, it is possible to expand the functional range of QCLs.

Second order processes, as there are second harmonic generation, sum frequency generation and difference frequency generation have already been demonstrated in InGaAs/InAlAs based QCLs. [38, 10] From devices based on the GaAs/$Al_xGa_{1-x}As$ material system up to date only the emission of second harmonic light was observed. [39] Even third harmonic generation was observed in $In_{0.7}Ga_{0.3}As/In_{0.4}Al_{0.6}As$ heterostructures. [40] All these effects allow to access additional wavelength ranges of the emitted light. Since QCLs are based on intraband transitions, they are an interesting tool for the investigation of nonlinear effects because the energy of the second harmonic photons is still below the bandgap energy of the materials and therefore the nonlinear light is not reabsorbed in the crystal.

5.1 Electromagnetic Waves in Nonlinear Media

This section investigates solutions to the wave equation for electromagnetic waves in nonlinear media. As sketched in figure 5.1 three effects can be observed in this case, namely second harmonic generation, sum frequency

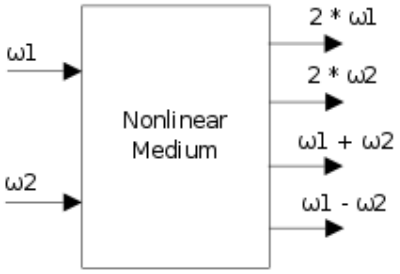

Figure 5.1: Nonlinear Light Generation in Media with 2nd Order Susceptibility

generation and difference frequency generation. Later ones only occur, when the inciding light consists of two different spectral parts.

Within the linear theory it is sufficient to model the material's influence on electromagnetic waves by the use of a constant susceptibility (χ), which is a proportional factor between the electric field ($\mathbf{E}$) and the polarization ($\mathbf{P}$). This relation is presented in term 5.1, where $(1 + \chi)$ is called the relative susceptibility.

$$\mathbf{D} = \epsilon_0 \mathbf{E} + \mathbf{P} = \epsilon_0 (1 + \chi) \mathbf{E} \tag{5.1}$$

When dealing with nonlinear effects the polarization vector can be expanded as a Taylor series like in expression 5.2. [17]

$$\mathbf{P} = \chi_{ij}^{(1)} \mathbf{E}_j + \chi_{ijk}^{(2)} \mathbf{E}_j \mathbf{E}_k + \dots \tag{5.2}$$

The starting point for further considerations is the wave equation, presented in term 5.3. It is modified for materials which feature a 2nd order susceptibility ($\mathrm{P}^{(2)}$). [17]

$$\Delta \mathbf{E} - \frac{\epsilon}{c_0^2} \frac{\partial^2 \mathbf{E}}{\partial t^2} = \mu_0 \frac{\partial^2 \mathbf{P}^{(2)}}{\partial t^2} \tag{5.3}$$

Using a simple plane wave ansatz as in term 5.4, which consists of two complex conjugated (c.c.) exponential wave functions with real amplitudes ($\mathbf{E}$), the 2nd order polarization consists of two terms. Both, a constant component, which is not relevant for wave propagation, and a part with double frequency are stimulated by the electric field, as demonstrated in terms 5.5 to 5.7.

$$\mathbf{E}(t) = \mathbf{E}e^{\iota\omega t} + c.c. \tag{5.4}$$

$$\mathbf{P}(t) = \frac{1}{2}\epsilon_0\chi^{(2)}\mathbf{E}(t)\mathbf{E}(t) \tag{5.5}$$

$$= \frac{1}{2}\epsilon_0\chi^{(2)}\mathbf{E}^2\left[1 + e^{\iota\omega t}e^{\iota\omega t} + c.c.\right] \tag{5.6}$$

$$= \frac{1}{2}\epsilon_0\chi^{(2)}\mathbf{E}^2\left[1 + e^{\iota 2\omega t} + c.c.\right] \tag{5.7}$$

The same scheme can be applied when dealing with electromagnetic waves that consist of at least to parts with different wavelengths. Solving the wave equation for term 5.8 leads to expression 5.9. It describes an electromagnetic wave that has components of the two original frequencies and two parts at the double frequencies as well as sum and difference frequency terms. [17]

$$\mathbf{E}(t) = \mathbf{E}e^{\iota\omega_1 t} + \mathbf{E}e^{\iota\omega_2 t} + c.c. \tag{5.8}$$

$$\mathbf{P}(t) = \frac{1}{2}\epsilon_0\chi^{(2)}\mathbf{E}^2\left[1 + e^{\iota 2\omega_1 t} + e^{\iota 2\omega_2 t} + 2e^{\iota(\omega_1+\omega_2)t} + 2e^{\iota(\omega_1-\omega_2)t}\right] \tag{5.9}$$

The 2nd order susceptibility ($\chi^{(2)}$) appears in all those terms as factor between electric field and polarization. It can only differ from zero in non point symmetric crystals, such as III-VI semiconductor compounds.

As shown in the preceding paragraphs, the higher powers of the electric field result in higher harmonic terms for every plane wave ansatz. Furthermore it is noteable that the wavevector (k) is different for fundamental and second harmonic components. [17, 41]

The second order coefficients of the nonlinear susceptibility are listed in

table 5.1 for various materials that are used for nonlinear optical devices. GaAs would provide the biggest 2^{nd} order susceptibility by far.

Material	**2^{nd} order coefficients**
KTP ($KTiOPO_4$)	$\lvert\chi^{(2)}_{31}\rvert$ = 13e-12 m/V
	$\lvert\chi^{(2)}_{32}\rvert$ = 10e-12 m/V
	$\lvert\chi^{(2)}_{33}\rvert$ = 27e-12 m/V
	$\lvert\chi^{(2)}_{15}\rvert$ = 12e-12 m/V
	$\lvert\chi^{(2)}_{24}\rvert$ = 15e-12 m/V
$LiNbO_3$	$\chi^{(2)}_{22}$ = 5.2e-12 m/V
	$\chi^{(2)}_{31}$ = -9.7e-12 m/V
	$\chi^{(2)}_{33}$ = -88e-12 m/V
GaAs	$\lvert\chi^{(2)}_{14}\rvert$ = 270e-12 m/V

Table 5.1: 2^{nd} Order Coefficients of Susceptibility, Values from [17]

5.2 Nonlinear Processes in Quantum Cascade lasers

The preceding section explained the nonlinearities that can be found in bulk GaAs. As an alternative the nonlinearity of intersubband transitions can be used as a source for nonlinear effects. The following sections show concepts that are used to achieve second harmonic generation in QCLs.

5.2.1 Devices on $\langle 111 \rangle$ oriented Substrates

One chance to generate nonlinear light in QCLs is to use the 2^{nd} order susceptibility of the material. According to the material parameters given in table 5.1, GaAs shows strongly nonlinear behaviour compared to other materials. [17] The index 14 given in the table mentioned above, is the short form for all tensor components of the susceptibility, whose indices are different from each other ($\chi^{(2)}_{123} = \chi^{(2)}_{213} = \chi^{(2)}_{132} = \chi^{(2)}_{231}$). Recalling equation 5.2 nonlinear polarization can only be excited when two projections to principal crystalline

axis of the electric field are different from zero. [42]

Therefore the semiconductor heterostructure needs to be grown on an $\langle 111 \rangle$ oriented substrate. The operation of such lasers has already been demonstrated in the $Al_xGa_{1-x}As$ and in the $In_{0.7}Ga_{0.3}As/In_{0.4}Al_{0.6}As$ material systems. [42, 43] The main drawback of these devices is the challenging growth, which results in worse quality of the grown material.

The devices discussed in this work are grown on $\langle 100 \rangle$ substrate like most other QCLs. For this geometry the electric field of laser emission coincides with the $\langle 100 \rangle$ direction of the semiconductor crystal, which means that the nonlinear susceptibility of the bulk material can't be used for second harmonic generation. The mechanism that is used in these devices is explained in the following paragraphs.

5.2.2 Nonlinearities in Quantum Wells

Shortly after advances in the MBE technique allowed to produce semiconductor heterostructures with good quality concerning composition and doping, nonlinear light generation from electrons excited to higher states in quantum wells was investigated. [44, 45] In these experiments carriers were excited by the use of CO_2 lasers. The same effect can be observed in electrically pumped QCLs. Both second and third harmonic light generation has been demonstrated. [38, 46, 47, 40] These nonlinearities of the quantum wells can also be tuned for other wavelength regions. With the use of a dual wavelength QCL difference frequency generation in the terahertz region was realized. [10]

Because the nonlinear behavior results from states of the quantum wells in the active region, it can be used to generate higher harmonics in QCLs grown on $\langle 100 \rangle$ substrates. In order to have matrix elements, which differ from zero, the quantum well must be asymmetric. In QCLs this is always the case because the conduction band profile of the heterostructure is tilted due to the applied electric field.[45]

Figure 5.2 shows the active region of sample H149. An additional state, labeled as state 5, above the injector level can be found. In fact there are more states that lie close to state 5, but the dipole matrix elements are 4 orders of

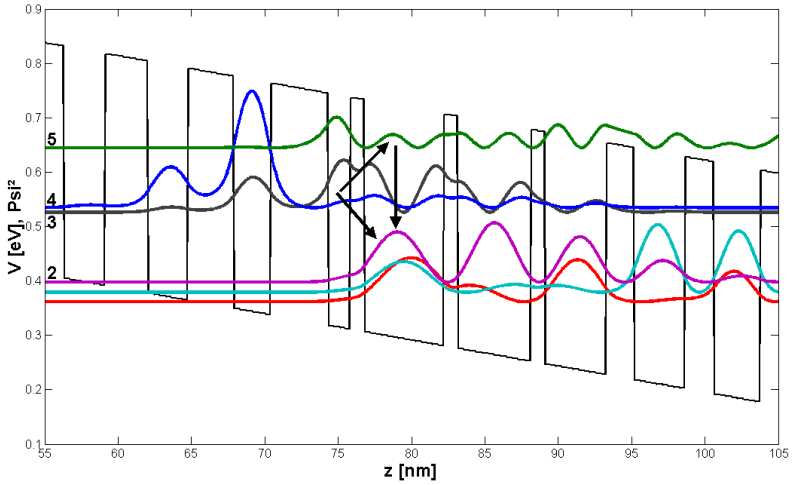

Figure 5.2: Optical transitions due to additional states in H149. The fundamental lasing transition takes place between level 3 and 2. Furthermore electrons can be excited to level 5 and produce second harmonic light, when relaxing to level 2

magnitude below the ones for the transitions to and from state 5. The arrows in the figure mark the important transitions that lead to fundamental and second harmonic emission. In material systems with deeper wells it would also be possible to have a second triplet of states that contributes to second harmonic emission. [48]

As mentioned in section 2.5.1 the transition rate obtained by Fermi's Golden Rule is proportional to the square of the dipole matrix element for given initial and final states. Term 2.20 provides the mathematical expression, which is evaluated for the discretized problem by a computer simulation. The dipole matrix elements that were obtained are presented in table 5.2.

It is remarkable that the matrix element for the $3 \rightarrow 5$ transition is nearly as large as for the $3 \rightarrow 2$ transition. This results in high threshold current densities due to the resonant re-absorption but also high values of $\chi^{(2)}$. [23]

Transition	Energy (meV)	Matrix Element (nm)
$4 \rightarrow 2$	136.3	0.71058
$3 \rightarrow 2$	127.9	-0.97802
$3 \rightarrow 1$	146.8	0.53153
$3 \rightarrow 5$	118.9	-0.90932
$5 \rightarrow 2$	246.8	0.70401

Table 5.2: Optical Transitions in H149

5.2.3 2nd Order Susceptibility

The preceding section explained the origin of nonlinear optical effects in quantum well structures. These can be described with an abstract 3 level system. In the case of GaAs/$Al_xGa_{1-x}As$ based QCLs the 3 levels of interest are the upper and lower laser level and another bound state above the upper laser level. [49] As shown in equation 5.2 the second order susceptibility is proportional to the ratio between nonlinear polarization and the square of the electric field.

An approximation for the second order susceptibility is given in term 5.10. There is a linear dependence on the carrier concentration (N_e) and on the product of the dipole matrix elements (μ_{if}) that are associated with the transitions between the 3 levels mentioned above. The denominator of the second fraction depends on the energies of the photons ($\hbar\omega$ and $2\hbar\omega$), on the differences of the state's energies and on the transition broadenings (γ_{if}). [49, 50]

$$\chi^{(2)} \propto \frac{N_e e^3}{\epsilon_0} \frac{\mu_{23}\mu_{35}\mu_{25}}{(\hbar\omega - \Delta E_{32} - \iota 2\gamma_{32})\,(2\hbar\omega - \Delta E_{25} - \iota 2\gamma_{25})} \tag{5.10}$$

Using the matrix elements and transition energies listed in table 5.2 the second order susceptibility of the semiconductor heterostructure H149 calculates to 5510e-12 m/V, which is significantly higher than the value for bulk GaAs (270e-12 m/V). Transition broadenings were neglected in this calculation.

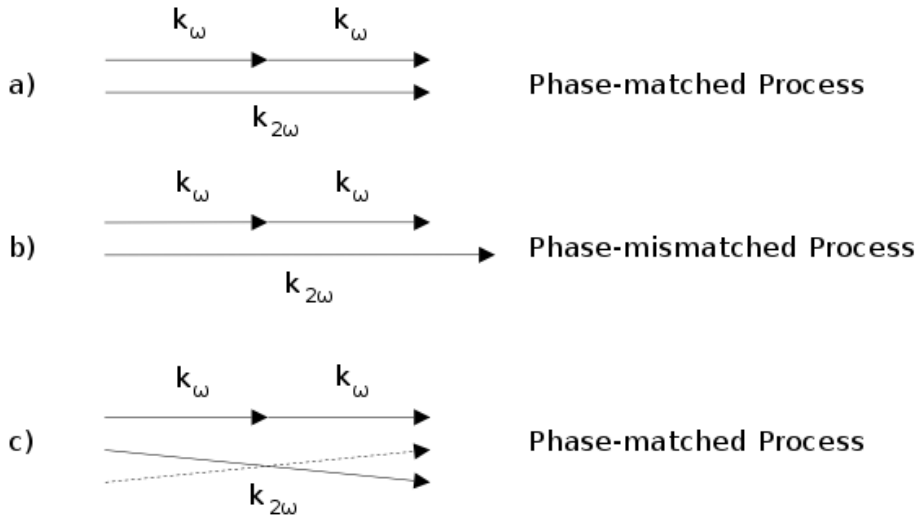

Figure 5.3: Phase-matched and -mismatched SHG Processes

5.3 Phase Mismatch

Electromagnetic waves are not only characterized by the frequency, which can be explained intuitively as period in time, but also by the wavevector which describes the spatial period. The wavevector for plane waves is presented in term 5.11. It depends on the effective refractive index (n_{eff}) and on the angular frequency (ω).

$$k = \frac{n_{eff}\omega}{c_0} \tag{5.11}$$

For an ideal medium without dispersion two wavevectors of the fundamental light would correspond to one wavevector of the second harmonic. Such a nonlinear light generation process, as sketched in figure 5.3a would be phase-matched. Unfortunately this implies the equality of the two effective refractive indices, which can't be fulfilled in the mid-infrared regime.

In dispersive media the two options shown in figures 5.3b and 5.3c can occur. Either there can be no phase-match at all and therefore the process takes place at low efficiencies, or the process is phase-matched but the wavevectors include a certain angle. [41]

If there is a phase mismatch, the second harmonic light propagates with a velocity that is different from the velocity of the driving nonlinear polarization, which changes instantaneous with the electric field, as shown in expression 5.2. In such a case energy can only be transferred to the electromagnetic wave in small regions, where the phase terms of the electromagnetic wave and the polarization term match. Therefore the efficiency of this process is limited. [51, 41]

5.3.1 Phasematch Gratings

In the case of mid-infrared signals the refractive index is larger for signals with shorter wavelengths. Therefore the model given in the preceding section would lead to wave propagation with phase-mismatch.

Gratings which are etched into the waveguide structure of the laser device represent a periodic modulation of the effective refractive index. This results in an additional Δk for the second harmonic signal. The effect of the grating on the wavevector can be expressed as in term 5.12, where Λ_G corresponds to the period of the grating. [17]

$$\Delta k = \frac{2\pi}{\Lambda_G} \tag{5.12}$$

When dealing with resonator structures, electromagnetic waves travelling in opposite directions can be found. Two options arise from these considerations. First the grating can be used to couple fundamental light with second harmonic light, which travels in the opposite direction, as shown in figure 5.4a. Such devices have also been investigated, but are not discussed here in detail. Another approach is to achieve phasematch between fundamental and second harmonic waves, which propagate in the same direction, as shown in figure 5.4b. This is the approach that was used for the devices presented in this work.

Using equations 5.11 and 5.12 the grating period (Λ_G) that is necessary to compensate the phase-mismatch can be calculated as a function of wavelength (λ_{SH}) and effective refractive indices for fundamental light ($n_{eff,F}$) and second harmonic light ($n_{eff,SH}$). The resulting relation is shown in term 5.13.

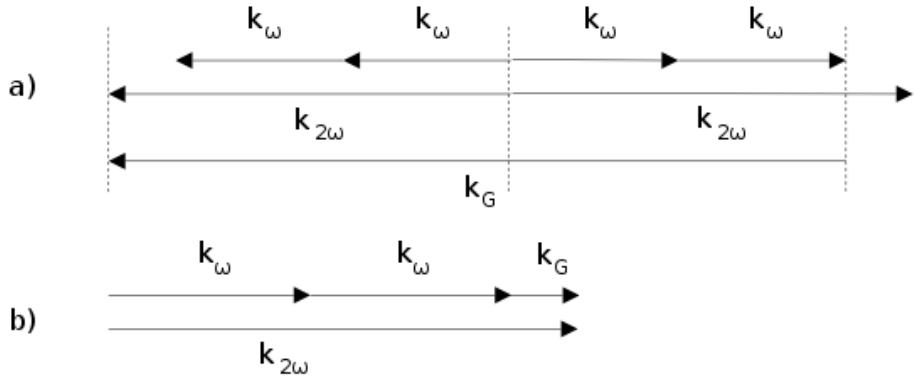

Figure 5.4: Phasematch Gratings

$$\Lambda_G = \frac{\lambda_{SH}}{n_{eff,SH} - n_{eff,F}} \tag{5.13}$$

Electromagnetic waves with a wavelength around 5 μm are not confined in vertical direction by the contrast of the refractive index between the $Al_{0.9}Ga_{0.1}As$ and the highly doped GaAs layers of the waveguide. Therefore the intensity of the second harmonic light is concentrated within the 2.35 μm thick core layers of the waveguide. According to equation 5.13 the grating should be around 27 μm, but this result strongly depends on the effective refractive indices and the carrier concentration. However this calculation isn't precise because the refrative index as well as the exact doping concentration are not known.

5.4 QCLs with Phase-Match Gratings

In compliance with the estimation, made in the preceding section, QCL devices with grating periods between 22 and 30 μm were fabricated. To keep the degrees of freedom within certain limits, a common width of 30 μm was chosen. Threshold current density and grating period as well as geometric parameters of the devices with PMG are summarized in table 5.3.

Device		Length (mm)	Grating Period (μm)	Threshold (kA/cm^2)	Conv. Eff. $\mu W/W^2$
H149I B1	P1	2	26	9.2	
	P2	2	28	10.9	33.7
	P3	2	22	8.9	19.7
	P4	2	24	10.6	14.3
	P5	2	28	10.3	
	P6	2	22	10.2	46.1
	P7	2	26	10.8	
	P8	2	30	13.7	9.6
H149I B2	P1	1.57	24	7.0	20.0
	P2	1.57	30	12.4	30.9
	P3	1.57	26		
	P4	1.57	22	7.3	20.1
	P5	1.57	28	6.4	21.2
	P6	1.57	24		
	P7	1.57	30	6.4	25.0
	P8	1.57	26	7.0	41.9

Table 5.3: QCL Devices with Phasematch Grating - Ridge Width 30 μm

5.4.1 Far Fields

Figure 5.5 presents a typical farfield profile of the second harmonic light in vertical direction of a QCL based on the material H149. There are two peaks, which appear under an angle of $\pm 30°$ with respect to the peak of the fundamental signal. The sharp edge at -30° is due to the limited size of the window in the cryostat.

Using the law of refraction (equation 5.14) the angle between fundamental and second harmonic light inside the waveguide structure calculates to 8.2° . [52]

$$\frac{\sin(\alpha_1)}{\sin(\alpha_2)} = \frac{n_2}{n_1} \tag{5.14}$$

A clear evidence for phase matching was not found in the samples, described above. All processed ridges showed second harmonic generation with conversion efficiencies in the 10-50 $\mu W/W^2$ range. Finer grids and extensions

to a broader range will be necessary to deepen our understanding of the light matching mechanisms involved.

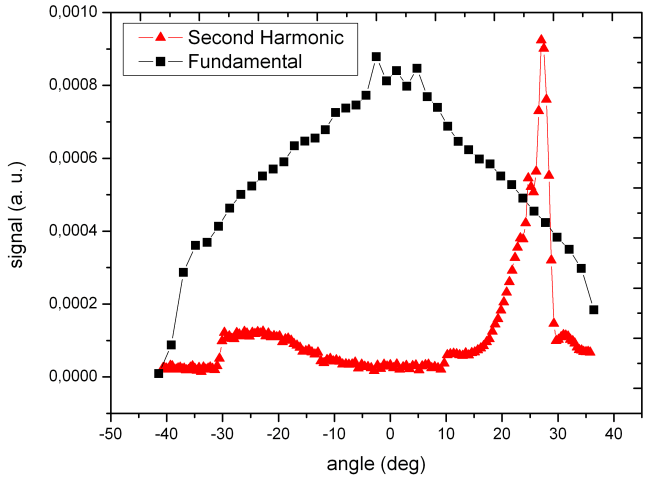

Figure 5.5: Farfield profiles for H149 samples. While the farfield of the fundamental light shows a Gaussian form, the second harmonic features two peaks which arise at $\pm 30°$.

5.4.2 Spectra of the Devices

Figures 5.6 and 5.7 show the spectral behavior of a set of QCL devices investigated. The devices from B1 exhibited narrow emission bandwidths, comparable to spectra of lasers with DFB gratings. This could be caused either by coupling between the electromagnetic mode and the grating or because of high losses, which allow lasing only for one mode.

In contrary the devices of B2 featured many Fabry Perot modes, as expected for situations, where no coupling between light and grating occurs. This difference could be attributed to the shorter length of the laser cavities, which of course results in a shorter interaction length between grating and light.

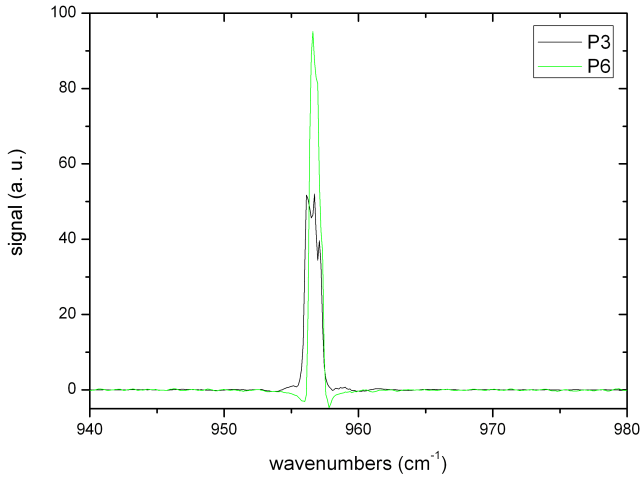

Figure 5.6: Spectra of the Fundamental Modes from H149I B1. The ridge waveguide has a length of 2mm and a width of 30 μm.

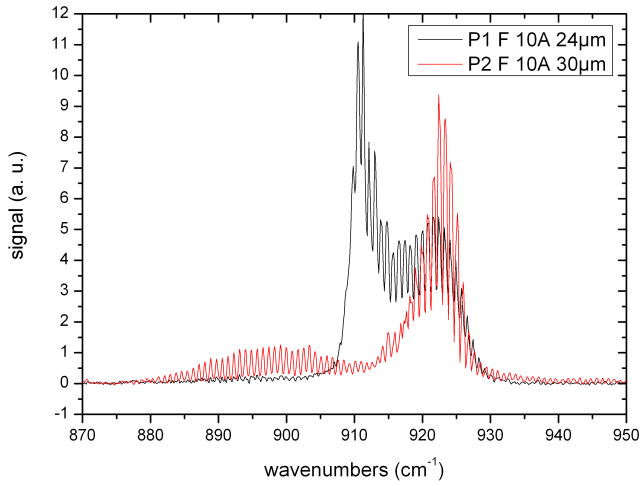

Figure 5.7: Spectra of the Fundamental Modes from H149I B2. The length of these devices is 1.57mm, while the width of the waveguides is 30 μm.

As shown in figure 5.8 the spectral parts of second harmonic generation appear exactly at the doubled wavenumber of the fundamental modes. The cuts near 1825, 1830 and 1845 wavenumbers are absorption lines of gases in the optical path of the measurement setup.

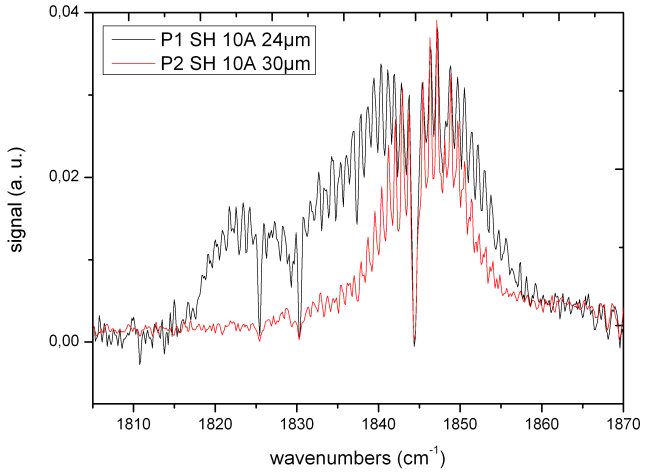

Figure 5.8: Spectra of the second harmonics from H149I B2. These devices are 1.57mm long and 30 μm wide and had grating periods of 24 and 30 μm.

5.4.3 Calculation of Conversion Efficiency

Conversion efficiency was chosen as a figure of merit to compare different devices. It is defined as the slope of the relation between second harmonic power and the square of fundamental power, as shown in term 5.15. From a mathematical point of view this relation should be linear, resulting in a constant slope. As shown in figure 5.9 the experimental results are in good agreement with theses considerations. However some devices featured kinks, which could be attributed to changes of the fundamental mode profile.

$$\text{conv. eff.} = \frac{P_{SH}}{P_F^2} \tag{5.15}$$

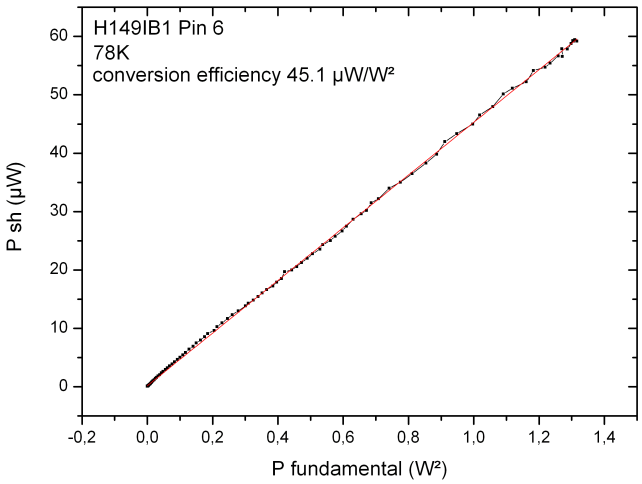

Figure 5.9: Conversion Efficiency (P_{SH}/P_F^2) for H149 B1 P6 (45.1 $\mu W/W^2$)

The conversion efficiencies that were obtained for the devices of H149 with phasematch gratings are plotted in figure 5.10. There seems to be no relation between the period of the gratings and the amount of converted light. It rather seems that these data points are scattered randomly.

5.4.4 Threshold of the Devices

In Figure 5.11 the thresholds of all devices with phase match gratings are plotted against the grating period. It can be seen that the second bar shows noticeably lower threshold values.

One influencing factor might be a difference in the quality of the fabry perot mirrors of the two bars. Because of the thick gold layer on top, the cleaved facets all looked somewhat rough. Therefore there might be a difference concerning the losses, when comparing the two laser bars.

A second effect, that may lead to this shift in threshold current density can be caused by the longer interaction length between the fundamental mode and the PMG. There must be some interaction between the waveguide

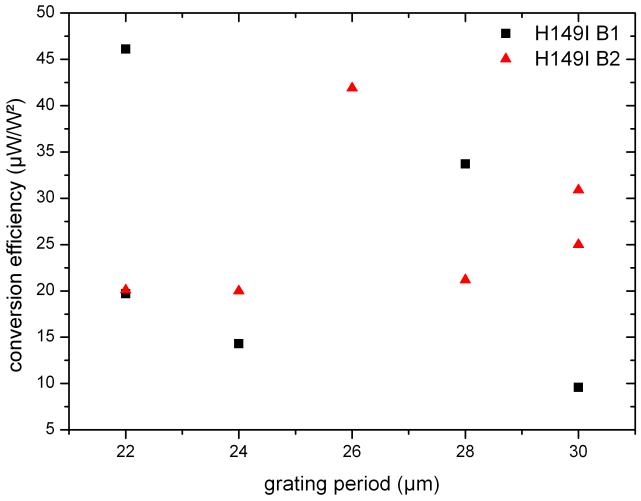

Figure 5.10: Conversion Efficiencies (P_{SH}/P_F^2) for Sample H149 with Phasematch Grating

gratings and the fundamental modes. When the losses due to the gratings become nearly as high as the laser gain only one fabry perot mode gets net gain. As seen in figures 5.6 and 5.7 bar 1, which has the longer device length, showed more narrow bandwidths compared to bar 2. It is not possible to locate the main problem based on the experimental results, which are available up to now.

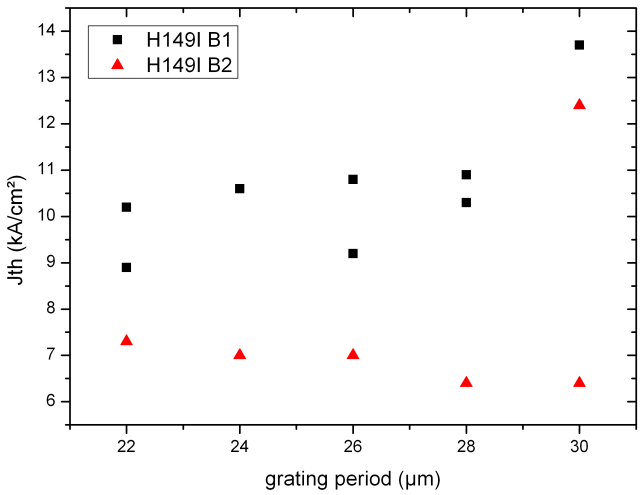

Figure 5.11: Thresholds for Sample H149 with Phase-match Grating. The devices of Bar 2 showed noticeable lower thresholds.

Chapter 6

Summary and Outlook

QCLs are versatile coherent sources for the mid-infrared regime. In contrast to conventional bandgap laser diodes the emission wavelength can be designed within a wide range. In order to expand the wavelength range nonlinear effects like second and third harmonic generation were studied. Because fundamental and second harmonic mode experience different refractive indices their propagation directions are not identical, which results in complex farfield patterns of the second harmonic signal.

This work presents the first approach to adjust the effective refractive indices for fundamental and second harmonic mode in a way to allow the same propagation direction for both fields by using phase-match gratings. The ridge waveguide of the QCL devices that were fabricated and characterized was modified with surface gratings that were supposed to allow phasematching. Expected results were a narrow farfield pattern of the second harmonic signal and higher conversion efficiencies because the phasematched overlap of the two electromagnetic waves should be spread to larger regions in the waveguide.

The devices that were fabricated and measured up to now didn't show a clear relation between the grating period and conversion efficiency or farfield profile. Two possible explanations arise from the experimental results, why no effects were observed that could unambiguously be attributed to the phase-match gratings. On the one hand the grating periods could be chosen

unfortunate due to uncertainties in the effective refractive indices. On the other hand the coupling between light and grating might be to low, so that the effect of the grating can not be seen in the measurements.

Nevertheless nonlinear effects in QCLs will remain interesting fields of research. These devices can be optimized further concerning waveguide design and processing. Also it will be a challenging topic to demonstrate other nonlinear effects, for example difference frequency generation or the emission of higher harmonics.

List of Figures

List of Tables

Bibliography

[1] J. Faist, F. Capasso, D.L. Sivco, C. Sirtori, A.L. Hutchinson, and A.Y. Cho. Quantum cascade laser. *Science*, 264(5158):553–556, 1994.

[2] R. Köhler, A. Tredicucci, F. Beltram, H.E. Beere, E.H. Linfield, A.G. Davis, D.A. Ritchie, R.C. Jotti, and F. Rossi. Terahertz semiconductorheterostructure laser. *Nature*, 417:156–159, 2002.

[3] J. Faist, F. Capasso, C. Sirtori, D.L. Sivco, and A.L. Hutchinson. Continuous wave operation of a vertical transition quantum cascade laser above T=80 k. *Applied Physics Letters*, 67(21):3057–3059, 1995.

[4] J. Faist, F. Capasso, C. Sirtori, D.L. Sivco, J.N. Baillargeon, A.L. Hutchinson, S.G. Chu, and A.Y. Cho. High power mid-infrared ($\lambda \approx 5\mu m$) quantum cascade lasers operating above room temperature. *Applied Physics Letters*, 68(26):3680–3682, 1996.

[5] H. Page, C. Becker, A. Robertson, G. Glastre, V. Ortiz, and C. Sirtori. 300 k operation of a GaAs-based quantum-cascade laser at $\lambda \approx 9\mu m$. *Applied Physics Letters*, 78(22):3529–3531, 2001.

[6] W. Schrenk, N. Finger, S. Gianordoli, E. Gornik, and G. Strasser. Continuous-wave operation of distributed feedback AlAs/GaAs superlattice quantum-cascade lasers. *Applied Physics Letters*, 77(21):3328–3330, 2000.

[7] M.P. Semtsiv, M. Wienold, S. Dressler, and W.T. Masselink. Short-wavelength ($\lambda \approx 3.05\mu m$) inp-based strain-compensated quantum-cascade laser. *Applied Physics Letters*, 90, 2007.

[8] J. Devenson, R. Teissier, O. Cathabard, and A.N. Baranov. InAs/AlSb quantum cascade lasers emitting below 3 μm. *Applied Physics Letters*, 90(111118), 2007.

[9] C. Sirtori, P. Kruck, S. Barbieri, P. Collot, and J. Nagle. GaAs/AlGaAs quantum cascade lasers. *Applied Physics Letters*, 73(24), 1998.

[10] M.A. Belkin, F. Capasso, A. Belyanin, D.L. Sivco, A.Y. Cho, D.C. Oakley, C.J. Vineis, and G.W. Turner. Terahertz quantum-cascade-laser source based on intracavity difference-frequency generation. *Nature Photonics*, 1(5):288–292, May 2007.

[11] G. Bastard. *Wave mechanics applied to semiconductor heterostructures*. Halsted Press, 1988.

[12] M. Shur M. Levinshtein, S. Rumyantsev, editor. *Semiconductor Parameters Vol. 2*. World Scientific, 1999.

[13] J. Singh. *Quantum Mechanics*. John Wiley & Sons, Inc., 1997.

[14] M. A. Stroscio V. V. Mitin, V. A. Kochelap. *Quantum Heterostructures*. Cambridge University Press, 1999.

[15] R.Q. Yang and S.S. Pei. Novel type-II quantum cascade lasers. *Journal of Applied Physics*, 79(11):8197–8203, 1996.

[16] P. Harrison. *Quantum Wells, Wires and Dots*. John Wiley & Sons Ltd, 2000.

[17] G. A. Reider. *Photonik*. Springer-Verlag, 1997.

[18] J. Singh. *Electronic and Optoelectronic Properties of Semiconductor Structures*. Cambridge University Press, 2003.

[19] J. Faist, F. Capasso, D.L. Sivo, C. Sirtori, A.L. Hutchinson, and A.Y. Cho. Quantum cascade laser: An intersub-band semiconductor laser operating above liquid nitrogen temperature. *Electronics Letters*, 30(11):865–866, 1994.

[20] J. Faist, M. Beck, T. Aellen, and E. Gini. Quantum-cascade lasers based on a bound-to-continuum transition. *Applied Physics Letters*, 78(2):147–149, 2000.

[21] G. Strasser, S. Gianordoli, L. Hvozdara, W. Schrenk, K. Unterrainer, and E. Gornik. GaAs/AlGaAs superlattice quantum cascade lasers at $\lambda \approx 13\mu m$. *Applied Physics Letters*, 75(10):1345–1347, September 1999.

[22] C. Gmachl, F. Capasso, D.L. Sivco, and A.Y. Cho. Recent progress in quantum cascade lasers and applications. *Reports on Progress in Physics*, 64:1533–1601, 2001.

[23] C. J. Pflügl. *Quantum design of mid-infrared semiconductor lasers*. PhD thesis, Technische Universität Wien, 2005.

[24] E.D. Palik, editor. *Handbook of Optical Constants of Solids II*. Academic Press, Inc., 1991.

[25] M.K. Gunde and N. Maček. Infrared optical constants and dielectric response functions of silicon nitride and oxynitride films. *Physica Status Solidi (a)*, 183(2):439–449, 2001.

[26] W. Schrenk. *Distributed feedback quantum cascade lasers*. PhD thesis, TU Wien, 2001.

[27] C. Gmachl, J. Faist, J.N. Baillargeon, F. Capasso, C. Sirtori, D.L. Sivco, S.N. Chu, and A.Y. Cho. Complex-coupled quantum cascade distributed-feedback laser. *IEEE Photonics Technology Letters*, 9(8):1090–1092, 1997.

[28] W. Schrenk, N. Finger, S. Gianordoli, L. Hvozdara, G. Strasser, and E. Gornik. GaAs/AlGaAs distributed feedback quantum cascade lasers. *Applied Physics Letters*, 76(3):253–255, 2000.

[29] R.F. Kazarinov and R.A. Suris. Possibility of the amplification of electromagnetic waves in a semiconductor with a superlattice. *Soviet Physics - Semiconductors*, 5(4):707–709, October 1971.

[30] M.A. Herman and H. Sitter. *Molecular Beam Epitaxy*. Springer-Verlag, Berlin Heidelberg New York, 1989.

[31] R. Williams. *Modern GaAs Processing Methods*. Artech House, Inc., 1990.

[32] R.A. Levy, editor. *Microelectronic Materials and Processes*. Kluwer Academic Publishers, 1989.

[33] G.W. Chantry. *Long-wave Optics, Volume 2: Applications*. Academic Press, Inc., 1984.

[34] Hamamatsu Solid State Division. Characteristics and use of infrared detectors, 2004.

[35] P. Norton. HgCdTe infrared detectors. *Opto-Electronics Review*, 10(3):159–174, 2002.

[36] D.G. Avery, D.W. Goodwin, and A.E. Rennie. New infra-red detectors using indium antimonide. *Journal of Scientific Instruments*, 34:394–395, October 1957.

[37] R. Patzelt and H. Schweinzer. *Elektrische Messtechnik*. Springer-Verlag Wien New York, 1996.

[38] N. Owschimikow, C. Gmachl, A. Belyanin, V. Kocharovsky, D.L. Sivco, R. Colombelli, F. Capasso, and A.Y. Cho. Resonant second-order nonlinear optical processes in quantum cascade lasers. *Physical Review Letters*, 90(4), January 2003.

[39] C. Pflügl, M. Austerer, W. Schrenk, and G. Strasser. Second-harmonic generation in GaAs-based quantum-cascade lasers grown on $\langle 100 \rangle$ substrates. *Electronics Letters*, 41(24), November 2005.

[40] T.S. Mosely, A. Belyanin, C. Gmachl, D.L. Sivco, M.L. Peabody, and A.Y. Cho. Third harmonic generation in a quantum cascade laser with monolithically integrated resonant optical nonlinearity. *Optics Express*, 12(13):2972–2976, June 2004.

[41] R.W. Boyd. *Nonlinear Optics*. Academic Press, 1992.

[42] J.-Y. Bengloan, A. De Rossi, V. Ortiz, X. Marcadet, M. Calligaro, I. Maurin, and C. Sirtori. Intracavity sum-frequency generation in GaAs quantum cascade lasers. *Applied Physics Letters*, 84(12), March 2004.

[43] M. Giovannini, M. Beck, N. Hoyler, and J. Faist. Second harmonic generation in (111)-oriented inP-based quantum cascade laser. *Journal of Applied Physics*, 101(103107), 2007.

[44] M.K. Gurnick and T.A. De Temple. Synthetic nonlinear semiconductors. *IEEE Journal of Quantum Electronics*, 19(5):791–794, May 1983.

[45] M.M. Fejer, S.J.B. Yoo, R.L. Byer, A. Harwit, and J.S. Harris Jr. Observation of extremely large quadratic susceptibility at 9.6-10.8 μm in electric-field-biased AlGaAs quantum wells. *Physical Review Letters*, 62(9):1041–1044, February 1989.

[46] M. Austerer, C. Pflügl, A.M. Andrews, T. Roch, W. Schrenk, and G. Strasser. Second-harmonic generation in GaAs-based quantum cascade lasers. *Physica E*, 35:234–240, 2006.

[47] M. Austerer, C. Pflügl, S. Golka, W. Schrenk, A.M. Andrews, T. Roch, and G. Strasser. Coherent $5.35\mu m$ surface emission from a GaAs-based distributed feedback quantum-cascade laser. *Applied Physics Letters*, 88(1211104), 2006.

[48] C. Gmachl, A. Belyanin, D.L. Sivco, M.L. Peabody, N. Owschimikow, A.M. Sergent, F. Capasso, and A.Y. Cho. Optimized second-harmonic generation in quantum cascade lasers. *IEEE Journal of Quantum Electronics*, 39(11), November 2003.

[49] O. Malis, A. Belyanin, D.L. Sivco, J. Chen, A.M. Sergent, C. Gmachl, and A.Y. Cho. Recent progress in nonlinear quantum cascade lasers. In *Proceedings of SPIE*, volume 5738, pages 80–89, 2005.

[50] A. Belyanin, D. Liu, F. Xie, F. Capasso, and C. Gmachl. Theory of intracavity nonlinear processes quantum cascade lasers. In *Proceedings of SPIE*, volume 5738, pages 98–108, 2005.

[51] J.A. Armstrong, N. Bloembergen, J. Ducuing, and P.S. Pershan. Interactions between light waves in a nonlinear dielectric. *Physical Review*, 127(6):1918–1939, September 1962.

[52] W. Demtröder. *Experimentalphysik 2*. Springer-Verlag, 2004.

Acknowledgements

It would not be correct to finish such a work without mentioning all those in thanks, who made it possible for me to complete my studies with this thesis. First I want to thank my parents for making it possible for me to study at Vienna University of Technology and for supporting me during the last years.

Also I'm grateful to Prof. Gottfried Strasser, who gave me the chance to work on interesting topics and helped throughout the writing of this thesis. Especially I would like to emphasize the support of Maximilian Austerer for instructing me in theory as well as fabrication and characterization of quantum cascade lasers and who proof-read this thesis.

Research projects like this can't be done alone. Therefore I'd also like to mention the support of Aaron Maxwell Andrews and Pavel Klang, who grew the semiconductor heterostructures by molecular beam epitaxy and answered all my questions on the material. Furthermore I'm indebted to Werner Schrenk, Stephan Schartner, Michele Nobile, Elvis Mujagic and Leonard Hoffmann for their patient assistence and many valuable discussions.